Control of innate olfactory valence by segregated cortical amygdala circuits

James R. Howe[1,2,3,9], Chung-Lung Chan[1,9], Donghyung Lee[1], Marlon Blanquart[1], James H. Lee[1], Laurine Decoster[1], Haylie K. Romero[2,3,4], Abigail N. Zadina[5,†], Mackenzie E. Lemieux[6], Fergil Mills[6,††], Paula A. Desplats[3,4,7], Kay M. Tye[1,6,8], & Cory M. Root[1,*]

[1] Department of Neurobiology, University of California, San Diego, La Jolla, CA 92093, USA

[2] Neurosciences Graduate Program, University of California, San Diego, La Jolla, CA 92093, USA

[3] Department of Neurosciences, University of California, San Diego, La Jolla, CA 92093, USA

[4] Center for Circadian Biology, University of California, San Diego, La Jolla, CA 92093, USA

[5] Zuckerman Mind Brain Behavior Institute, Columbia University, New York, NY, 10027, USA

[6] Salk Institute for Biological Sciences, La Jolla, CA 92037, USA

[7] Department of Pathology, University of California, San Diego, La Jolla, CA 92093, USA

[8] Howard Hughes Medical Institute, La Jolla, CA 92037, USA

[9] These authors contributed equally

[†] Current affiliation: Department of Neuroscience and Behavior, Barnard College of Columbia University, New York City, NY 10027, USA

[††] Current affiliation: Department of Neurobiology, University of Utah School of Medicine, Salt Lake City, UT 84112, USA

* To whom correspondence should be addressed:

Cory M. Root, PhD
University of California, San Diego
9500 Gilman Drive
3119 Pacific Hall
La Jolla, CA 92093-0357
cmroot@ucsd.edu

Abstract

Animals exhibit innate behaviors that are stereotyped responses to specific evolutionarily relevant stimuli in the absence of prior learning or experience. These behaviors can be reduced to an axis of valence, whereby specific odors evoke approach or avoidance responses. The posterolateral cortical amygdala (plCoA) mediates innate attraction and aversion to odor. However, little is known about how this brain area gives rise to behaviors of opposing motivational valence. Here, we sought to define the circuit features of plCoA that give rise to innate attraction and aversion to odor. We characterized the physiology, gene expression, and projections of this structure, identifying a divergent, topographic organization that selectively controls innate attraction and avoidance to odor. First, we examined odor-evoked responses in these areas and found sparse encoding of odor identity, but not valence. We next considered a topographic organization and found that optogenetic stimulation of the anterior and posterior domains of plCoA elicits attraction and avoidance, respectively, suggesting a functional axis for valence. Using single cell and spatial RNA sequencing, we identified the molecular cell types in plCoA, revealing an anteroposterior gradient in cell types, whereby anterior glutamatergic neurons preferentially express *VGluT2* and posterior neurons express *VGluT1*. Activation of these respective cell types recapitulates appetitive and aversive behaviors, and chemogenetic inhibition reveals partial necessity for responses to innate appetitive or aversive odors. Finally, we identified topographically organized circuits defined by projections, whereby anterior neurons preferentially project to medial amygdala, and posterior neurons preferentially project to nucleus accumbens, which are respectively sufficient and necessary for innate attraction and aversion. Together, these data advance our understanding of how the olfactory system generates stereotypic, hardwired attraction and avoidance, and supports a model whereby distinct, topographically distributed plCoA populations direct innate olfactory responses by signaling to divergent valence-specific targets, linking upstream olfactory identity to downstream valence behaviors, through a population code. This suggests a novel amygdala circuit motif in which valence encoding is represented not by the firing properties of individual neurons, but by population level identity encoding that is routed through divergent targets to mediate distinct behaviors of opposing appetitive and aversive responses.

INTRODUCTION

Innate behaviors are ubiquitous across the animal kingdom, allowing specific sensory stimuli to yield stereotypical behavioral responses even in the absence of learning or past experience. These behaviors include feeding, fighting, fleeing, and mating, among others, and many can be simplified onto an axis of positive or negative valence representing approach and avoidance. Innate behaviors are the result of evolutionary selection, guiding initial behaviors that can be updated by future experiences. Given that innate behaviors are genetically hardwired, it is thought they should be mediated by simple circuits with specified connections between layers of the nervous system. Innate behaviors are common across sensory modalities but are especially prominent in olfaction, whereby diverse chemical signals, critical to survival and reproduction, must be quickly and robustly detected and processed, in the absence of prior experience. For instance, predator odors represent a potentially imminent threat and necessitate a quick, decisive, aversive response[1]. Conversely, innately appetitive odors represent potentially rewarding stimuli like food or heterospecifics, inducing attraction[2]. These odors comprise a small subset of perceptible chemical space, and the detection of specific odorants is both species-specific and under genetic control[3-5].

Valence is a fundamental perceptual feature of olfaction[6]. Motivational valence can be defined as seeking or avoiding specific stimuli, and it is observed across sensory stimuli in both innate and learned responses. Multiple circuit motifs have been proposed to mediate such valence responses[7]. In the simplest form, labeled line motifs segregate information from sensation to action throughout the nervous system. This has been observed in the taste and somatosensory systems, as well as hints of labeled lines in the olfactory system, where individual glomeruli are necessary and sufficient for innate responses consistent with this model[8-10]. Many circuits are organized along divergent path motifs, where a region receives the same sensory input but instead acts akin to a switchboard, processing and sorting its output to distinct downstream targets to convey positive or negative signals. This motif is most associated with the BLA and associated learning processes[7, 11]. Still other circuits contain opposing components motifs, in which opposing inputs target a single effector region to control the balance of one target. It remains unclear which, if any, of these generalized circuit motifs are present in the olfactory system.

Olfactory sensation begins with olfactory sensory neurons (OSNs) in the olfactory epithelium (OE) that express a single receptor, projecting to spatially stereotyped glomeruli in the olfactory bulb (OB). Postsynaptic mitral/tufted cells within the OB project in parallel to third-order olfactory areas, including the posterolateral cortical amygdala (plCoA). Unlike in other third-order olfactory areas, such as piriform cortex, projections from individual glomeruli from the OB to plCoA are spatially restricted and stereotyped, consistent with genetically hardwired circuits[12, 13]. Past work has demonstrated that plCoA is necessary and sufficient for innate olfactory responses, with spatially ordered labeling of responsive neurons via immediate early gene labeling[14]. However, other work suggests that there is no spatial organization to odor responses or valence encoding in plCoA[15]. Thus, a further investigation of plCoA organization is necessary to understand how this structure controls innate olfactory responses.

Distinct brain areas employ distinct coding strategies to represent information. Neuronal ensembles within all other major olfactory regions observed thus far, such as the anterior olfactory nucleus, OB, OE, olfactory tubercle (OT), piriform cortex (PIR), and tenia tecta all generally perform sparse population encoding of odor identity, despite the major differences in neuronal composition, organization, and function between the six regions[15-21]. On the other hand, ensembles within amygdala subnuclei, most notably the basolateral amygdala (BLA), instead tend to represent the valence of stimuli instead, with considerable heterogeneity based on a given population's projection target, molecular identity, and topography[11, 22]. A complete investigation of the encoding properties and organization of plCoA is needed to determine how innate olfactory valence emerges from this region.

To identify the plCoA circuitry that underlies innate attraction and avoidance to odor, we investigated multiple intersecting scales of organization, from single cell transcriptomes and spatial gene expression, to circuit mapping, manipulation, and physiology. First, we used 2-photon calcium imaging to find that plCoA ensembles encode odor identity, but not valence. Next, we identify a functional gradient in plCoA where activation of anterior and posterior neurons drives responses of opposing valence. Next, we characterized the cell types within plCoA, identifying novel, molecularly defined populations specific to each domain of plCoA, which are respectively sufficient and partially necessary for innate olfactory valence. Further, we perform comprehensive projection mapping to identify downstream projection targets of plCoA, identifying projections to the medial amygdala (MeA) and nucleus accumbens (NAc) that are enriched based on molecular and topographic identity. Finally, manipulations of neuronal ensembles projecting to these targets are sufficient and necessary to control innate olfactory valence responses. Together, these findings identify a novel topographically distributed circuit from plCoA to MeA and NAc that controls innate olfactory aversion and attraction, respectively, consistent with a hybrid model mixing features of labeled lines and divergent path circuit motifs.

RESULTS

Population Encoding of Odor Identity in plCoA

To better understand how plCoA circuitry mediates innate attraction and aversion, we first decided to examine the relationship between its spatial organization and odor-evoked activity. Prior analysis of immediate early gene expression following minutes-long odor exposure suggests that activity in the anterior and posterior domains of plCoA could respectively mediate innate aversive and appetitive odor responses[14]. However, *in vivo* electrophysiology with high-density electrode arrays found no evidence for spatial organization or valence encoding in plCoA[15]. These two studies propose contradictory models of plCoA encoding properties that are both plausible, given that the former is common in the extended amygdala and insular cortex[23], and the latter is ubiquitous across olfactory regions[18]. We speculated that technical differences could be responsible for these opposing findings. Immediate early gene labeling has low temporal resolution and likely requires a high amount of neural activity to activate gene expression. On the other hand, the recording sites in the latter study appear biased towards the middle of plCoA, and odor was given for 2 seconds in interleaved trials, whereas attraction and

avoidance responses have been measured on a minutes-long timescale[14, 24]. Although it is unclear when the valence of an odor is first perceived, we wondered if the apparent contradictions in these studies could be resolved by applying a longer odor delivery protocol that better matches the timescale of behavioral readouts and balances spatial and temporal resolution.

Therefore, we developed an approach to image neural activity in plCoA with a modified odor delivery schedule, expressing GCamP8s targeted towards either the anterior or posterior subsection of plCoA and implanting a gradient-index relay (GRIN) lens above to allow *in vivo* imaging of calcium transients via head-fixed two-photon microscopy (**Figure 1A-C, S1A-B**). We then examined calcium responses in these mice during a long odor exposure, where odors were presented repeatedly in 20-trial blocks for 5 seconds each in counterbalanced order (**Figure 1D**). We chose two odorants of each innate valence: the appetitive odors 2-phenylethanol (2PE) and peanut oil (PEA), the neutral odors heptanol (HEP) and isoamyl acetate (IAA), and the aversive odors trimethylthiazoline (TMT) and 4-methylthiazoline (4MT)[14]. In total, we recorded Ca^{2+} signals from 345 neurons across 13 mice.

First, we pooled anterior and posterior plCoA neurons together and performed hierarchical clustering of their trial-averaged responses to the 6 odors to categorize odor responses in an unbiased manner (**Figure 1E**). Consistent with the previous *in vivo* electrophysiology study, we found that the majority of plCoA neurons did not seem to selectively respond to odors of one valence group (**Figure 1E-F**). Across mice, a majority of plCoA neurons did not reliably respond to any of the six odors, and activity was sparse: only 34.5% of plCoA neurons responded to 1 of the 6 odors and 10% to 2 odors, while a much smaller portion of plCoA neurons responded to 3 or more odors (**Figure 1G**). Further, we found no significant relationship between the valence of odor and proportion of responsive neurons, and no difference in the proportion responsive to the different odors across anterior and posterior plCoA, suggesting a lack of bias in responsiveness to aversive or appetitive odors across the anterior-posterior axis (**Figure 1H**).

We next attempted to quantify valence encoding by calculating a valence score for each neuron by subtracting the average integrated aversive odor response from the average integrated appetitive odor response and dividing this resulting difference in valence by the integrated odor response ($V = \frac{\Sigma_{appetitive} - \Sigma_{aversive}}{\Sigma_{total}}$). Although the valence score was more negatively skewed amongst anterior neurons than posterior ones, there was no significant difference in their distributions, indicating that anterior and posterior plCoA neurons do not broadly encode opposing appetitive and aversive responses (**Figure 1I**). Given that the innate aversive and appetitive behaviors evolve over time in freely moving animals, we wanted to assess if odor responses changed between early and late trials. Using a moving window of 5 trials, we examined if the proportion of neurons with significant aversive or appetitive valence scores differed over time in anterior or posterior plCoA but found no significant interaction between time and imaging location (**Figure 1J**).

Repeated olfactory stimuli, with the same odor, was used to asses potential changes in odor representation that evolve over a time scale more consistent with our behavioral assay, but

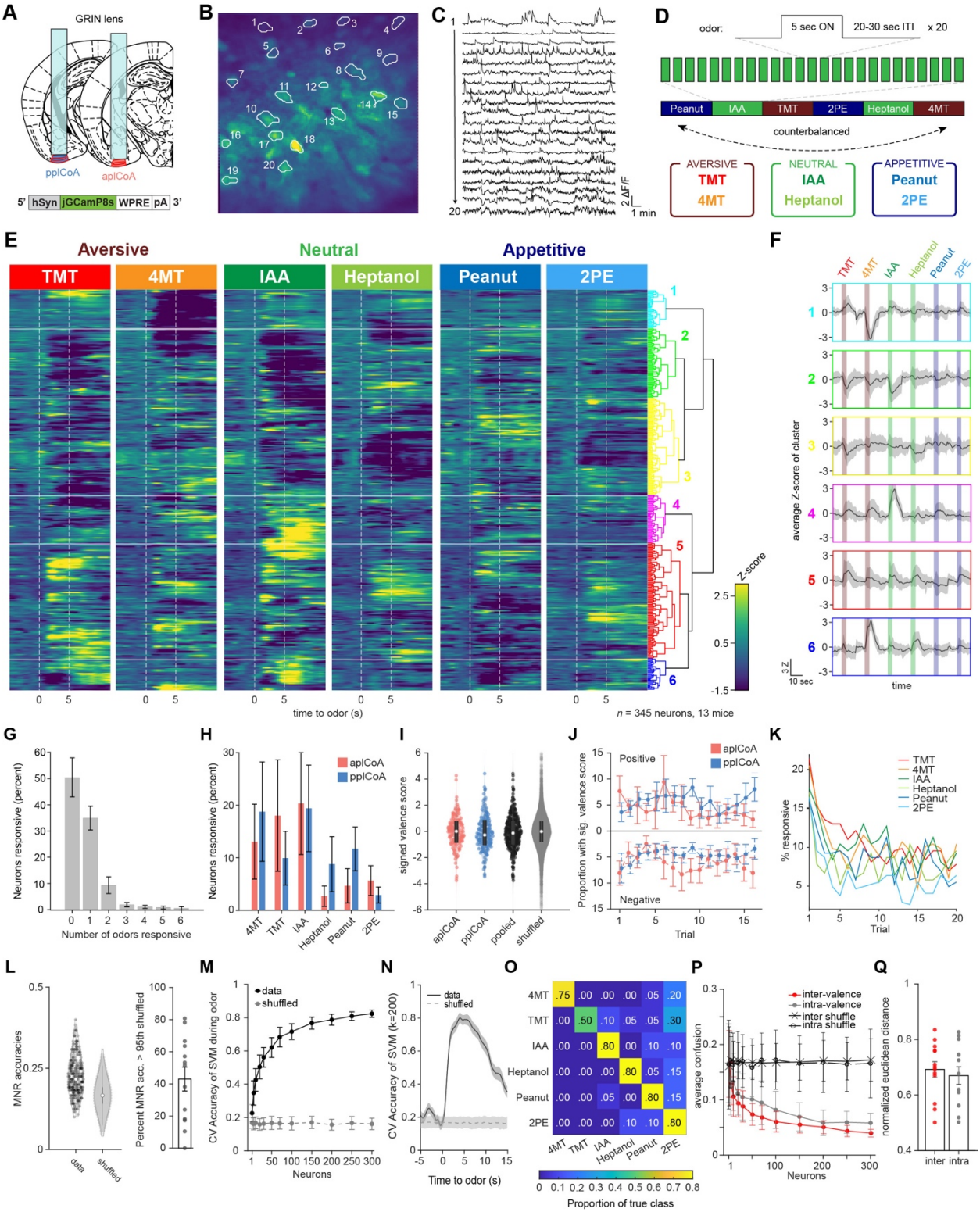

Figure 1. The plCoA encodes odors of innate-valence using a population code for odor identity.

(A) Schematic representation of virus injection and GRIN lens implantation into aplCoA or pplCoA for two-photon microscopy.

(B-C) Representative images (**B**) and traces (**C**) of fluorescence changes in individual neurons over an approximately 20-minute period that includes periods of odor stimulation.
(D) Schematic of odor exposure paradigm. Each trial presented 5 seconds of odor followed by a variable inter-trial interval (20-30s). Odors were present in blocks of 20 trials per odor, with 2 counterbalanced block schedules (1 & 2). Six odors were used: the appetitive odors 2-phenylethanol (2PE) and peanut oil (PEA), the neutral odors heptanol (HEP) and isoamyl acetate (IAA), and the aversive odors trimethylthiazoline (TMT) and 4-methylthiazoline (4MT).
(E) Heatmap of trial-averaged and Z-scored odor-evoked activity over time from pooled plCoA neurons. Responses are grouped by hierarchical clustering, with the dendrogram (right). Odor delivery marked by vertical red lines.
(F) Average of trial-averaged and Z-scored odor-evoked activity for each cluster concatenated. The order of color-coded blocks corresponds to the order of clusters in (**E**).
(G) Proportion of neurons responsive to different numbers of odors. Bars represent the mean across 13 animals and the error bars show SEM.
(H) Proportion responsive to each odor for aplCoA (red) or pplCoA (blue).
(I) Valence scores of individual neurons. White circles show the median of each distribution, whereas the gray rectangle shows the 25th-75th percentile range.
(J) Proportion of neurons with significant valence scores calculated as a function of trial number. Calculated with a 10-trial moving window. Top half shows those with significant positive valence scores, the bottom half shows those with significant negative valence scores.
(K) The percentage of neurons with responses (Z>2 for at least 5 frames) as a function of trial number for each odor.
(**L**) Left, MNR accuracies for all pooled plCoA neurons (data) and a control distribution where the training labels are shuffled (shuffled) in a violin plot. Right, proportion of neurons in each animal that have MNR accuracy greater than the 95th percentile of the shuffled MNRs.
(**M**) Cross-validated average accuracies of multinomial SVM's plotted as a function of the number of neurons used for training during the odor period. Circles represent the mean across 100 iterations of random sampling of neurons and error bars show the standard deviation.
(**N**) Cross-validated accuracy of ecoc-SVM classifiers for a 6-odor classification task trained using 200 neurons as a function of time. Lines indicate means and shaded areas show the standard deviation across 100 random samplings of 200 neurons from the pooled data, and shuffled training controls where the label vectors are randomly shuffled.
(O) An example confusion matrix for a multinomial SVM trained with 200 neurons.
(P) Comparison of inter-valence and intra-valence confusion across number of neurons used in training the classifiers. Filled circles show the average of the data across 100 iterations, open circles show shuffled controls.
(Q) The normalized average distance between odor pairs that have different valence (inter) or same valence (intra).
Across panels, ns, not significant. Additional specific details of statistical tests can be found in Supplemental Table 1.

198 this raises concerns about stability of odor delivery across trials and neuronal habituation. To
199 address this, we first assessed the reliability of odor delivery and neuronal responses across
200 trials. PID (Photo Ionization Detector) recordings of odor stimuli across trials revealed
201 moderately stable delivery of all odorants (**Figure S1C,D**). Neutral odors were the least stable
202 with a 29-39% decrease in PID detection between the first and last five trials, whereas the
203 attractive and aversive odors decreased by 15-18%. Although the odors do not entirely deplete
204 over time, these changes in odor concentration may affect physiological responses to odor.
205 Next, neuronal response reliability was assessed by examining the frequency of neurons
206 responding with a z score greater than 2 to each odor. With this criterion, the majority of
207 neurons responded to less than half of the trials, while a subset responded to as many as 17/20
208 trials (**Figure S1E,F**). Using a less stringent criteria for responsiveness (z score > 1), more
209 neurons appear to respond on more than half of the trials with a minority responding to all trials
210 (not shown). It is noteworthy that these response probabilities are lower than that observed by
211 Iurilli et al., using intermingled odor stimuli[15], indicating that repeated stimulus appears to
212 cause to some habituation in odor response, which may also be partly due to a decrease in odor
213 concentration. However, despite the weak reliability of individual neurons, the total number of
214 responsive neurons in the population remained fairly consistent across trials (approximately 5-
215 10%) after a decrease following the first two trials (**Figure 1K**). Thus, despite some changes in
216 representation across trials, we do not see the emergence of valence and this doesn't appear to
217 result from failure to deliver odor or stimulate neurons.

218 We further investigated odor encoding at the single neuron level using multinomial
219 regression (MNR) 6-odor classifiers trained on single neuron data and found that they perform
220 only marginally better than chance, suggesting that the majority of single plCoA neurons do not
221 broadly encode discriminatory information about odor identity (**Figure 1K**). Across mice, only
222 43.1% have overall classification rates above the 95th percentile of shuffled controls, indicating
223 that the majority of single plCoA neurons do not broadly encode discriminatory information
224 about odor identity. Interestingly, when comparing the ranked sub-accuracies for single odors
225 compared to shuffled controls, we found the discrepancy between data and shuffled controls to
226 be accentuated in the 2 highest performing sub-accuracies (**Figure S1G**). Quantifying the
227 proportion of neurons with sub-accuracies higher than the 95th percentile of the shuffled across
228 biological replicates, we found that the decrease of sub-accuracies down the rank falls
229 exponentially, rather than linearly (**Figure S1H**). This observation suggests that the individual
230 neurons examined here have little information about the odors tested. This may seem surprising
231 given that sparsely responsive neurons should carry highly specific information about odor
232 identity. However, it is important to note that we are under sampling the large stimulus space
233 (likely billions of odors), thus the neurons we sampled seem to carry little information about the
234 limited stimulus space we tested. It is also possible that faint reliability dilutes the averaged
235 signal used to decode from single neurons. Nonetheless, we do not find an enrichment for
236 neurons specific to odors of valence.

237 Since we did not observe any evidence of valence encoding at the single neuron level,
238 we next considered population level encoding. The plCoA neurons appear to primarily encode
239 odor identity in a sparse manner much like the other higher-order olfactory areas, known to use

a population code. In contrast to the poor single neuron classification, SVMs trained on population-level data vastly outperform the shuffled data, indicating good encoding of identity at the population level (**Figure 1M,N**). We further used a confusion matrix to ask whether training the classifier with a given odor could accurately predict the identity of another odor. In the matrix each row corresponds to a predicted class and each column corresponds to the actual class (**Figure 1O**). If the population level activity is similar between odor pairs, we expect the confusion to be higher than less similar pairs. The output of a confusion matrix yields a proportion of true class labels, whereby a high proportion indicates good prediction. We found no difference between the confusion rates for intra-valence classification or inter-valence classification, suggesting a lack of valence encoding at the population level (**Figure 1P**). The similarity between inter-valence and intra-valence confusion was mirrored when quantifying the range-normalized pairwise Euclidean distance across biological replicates (**Figure 1Q, S1I**). Thus, plCoA appears to encode odor identity in a population code like other higher order olfactory regions, with no apparent encoding of valence.

We next examined whether odor tuning varied with odor-evoked behavior during head fixation. Walking velocity was recorded on a treadmill-linked encoder during imaging trials, enabling analysis of odor-evoked locomotor responses and trial sorting based on behavioral patterns. To classify behavioral patterns, normalized walking velocity across trials was pooled and subjected to hierarchical clustering (**Figure S2A)**. This analysis revealed distinct odor-evoked locomotor responses with different temporal profiles (**Figure S2B)**. For example, cluster I displayed increased velocity early during the odor that continued for ~5 seconds after odor delivery, whereas cluster III displayed increased velocity beginning at odor termination. The majority of trials fell into cluster IV, which showed little change in odor-evoked walking velocity. To determine whether locomotor responses were odor specific, we compared cluster prevalence for each odor (**Figure S2C**) and the distribution of odor within clusters as a function of trial number (**Figure S2D**). Although we did not observe any reliable valence-specific behavioral responses to odor in head-fixed mice, we did observe divergent patterns of walking behavior unrelated to odor identity. To test whether these clusters of behavioral responses are associated with changes in odor representation, we analyzed neural activity based on its respective behavioral cluster for each trial (**Figure S2E,F**). Sorting the data by behavioral response type did not reveal any valence-specific responses, but did uncover systematic differences in neural activity. For example, in cluster I, when animals increase velocity at odor onset, we see a general decrease in odor-evoked activity. In contrast, the broadest responses to odors are found in cluster IV, where animals exhibit little change in behavior. Overall, we did not detect valence-specific behavioral or neural responses to odor in head-fixed mice.

A Functional Axis for Valence in plCoA

Since we did not observe clear evidence for valence encoding, we considered other organizational principles that could support appetitive and aversive behaviors. Spatial organization for valence processing has been previously observed in the insular cortex and BLA, whereby discrete subsections of the region contain neurons wired to preferentially signal positive or negative valence[11, 22, 25]. Given plCoA's spatially-ordered afferent projections

281 from OB, we next hypothesized that plCoA circuitry could still be organized along the anterior-
282 posterior (AP) axis to support attraction and aversion. If true, it follows that activation of small
283 ensembles of neurons along the AP axis should generate behavioral responses along a
284 corresponding axis of valence. We tested this prediction by expressing channelrhodopsin
285 (ChR2) in subsets of neurons at different positions along this axis and photostimulating them
286 during behavioral testing in the previously established four-quadrant open field arena[14].

287 Based on cytoarchitecture, we parcellated plCoA into three domains: the anterior plCoA
288 (aplCoA), a two-layered region on the ventral surface lateral to the anterior cortical amygdala,
289 the posterior plCoA (pplCoA), a three-layered region on the ventrolateral surface lateral to the
290 posteromedial cortical amygdala, and a middle zone (mplCoA) between them (**Figure 2A**)[14].
291 To determine the potential relationship between position on the anterior-posterior axis of plCoA
292 and evoked behavior, we performed optogenetic stimulation at points along this entire axis,
293 expressing channelrhodopsin (ChR2) [26]and implanting fibers into each zone (**Figures 2B-C,**
294 **S3A**). Behavioral response was assessed using the four-quadrant open field assay, where mice
295 freely explored a chamber with or without stimulation, and approach or avoidance was scored
296 with a performance index measuring quadrant occupancy relative to chance, as well as the
297 mean distance to the corner port. Mice were tested for a 10 minute baseline period followed by
298 15 minutes of closed loop optogenetic stimulation (470nm, increasing from 1-10 Hz as the
299 mouse proceeds closer to the corner port) in one quadrant (**Figure 2D**) as previously done [14].

300 Throughout the trial period, we observed a negative linear relationship between the
301 anterior-posterior position of photostimulation site and the valence of the behavior. The amount
302 of time spent in the stimulated quadrant as well as the distance to the corner port varied in
303 ChR2, but not eYFP-infected mice, whereby responses shifted from appetitive to aversive as
304 stimulation became more anterior (**Figure 2E-F**). We grouped these responses to determine
305 whether these opposing responses were specific to the identified plCoA zones. We found that
306 photostimulation in aplCoA significantly reduced time spent in the 'on' quadrant and increased
307 the average distance to the corner port during the treatment period, indicating activation of
308 aplCoA neurons is aversive and leads to avoidance of the quadrant paired with stimulation
309 (**Figure 2G-I**). We also found the opposite was true in pplCoA, where stimulation in that zone
310 instead increased the time in the 'on' quadrant and decreased average distance to the corner
311 port, indicating pplCoA neuron activation instead is appetitive and leads to attraction to the
312 stimulation quadrant (**Figure 2J-L**).

313 In the experiment described above, ChR2 was expressed in thousands of neurons, a
314 scale that is not physiologically representative. This led us to ask whether activating a sparse
315 ensemble of neurons in either the anterior plCoA (aplCoA) or posterior plCoA (pplCoA) would
316 evoke similar behavioral responses. To achieve sparse labeling, we used an immediate early
317 gene–based strategy to label odor-responsive neurons. The Arc-creER^{T2} mouse was previously
318 used in combination with Cre-dependent AAVs to label odor responsive neurons in plCoA for
319 broad activation [14]. We adapted this approach by targeting AAV-DIO-ChR2-eYFP to either the
320 anterior or posterior plCoA followed by tamoxifen induction and TMT exposure. The odor TMT
321 was used as because it labels neurons across the entire plCoA with this system [14]. Although

322

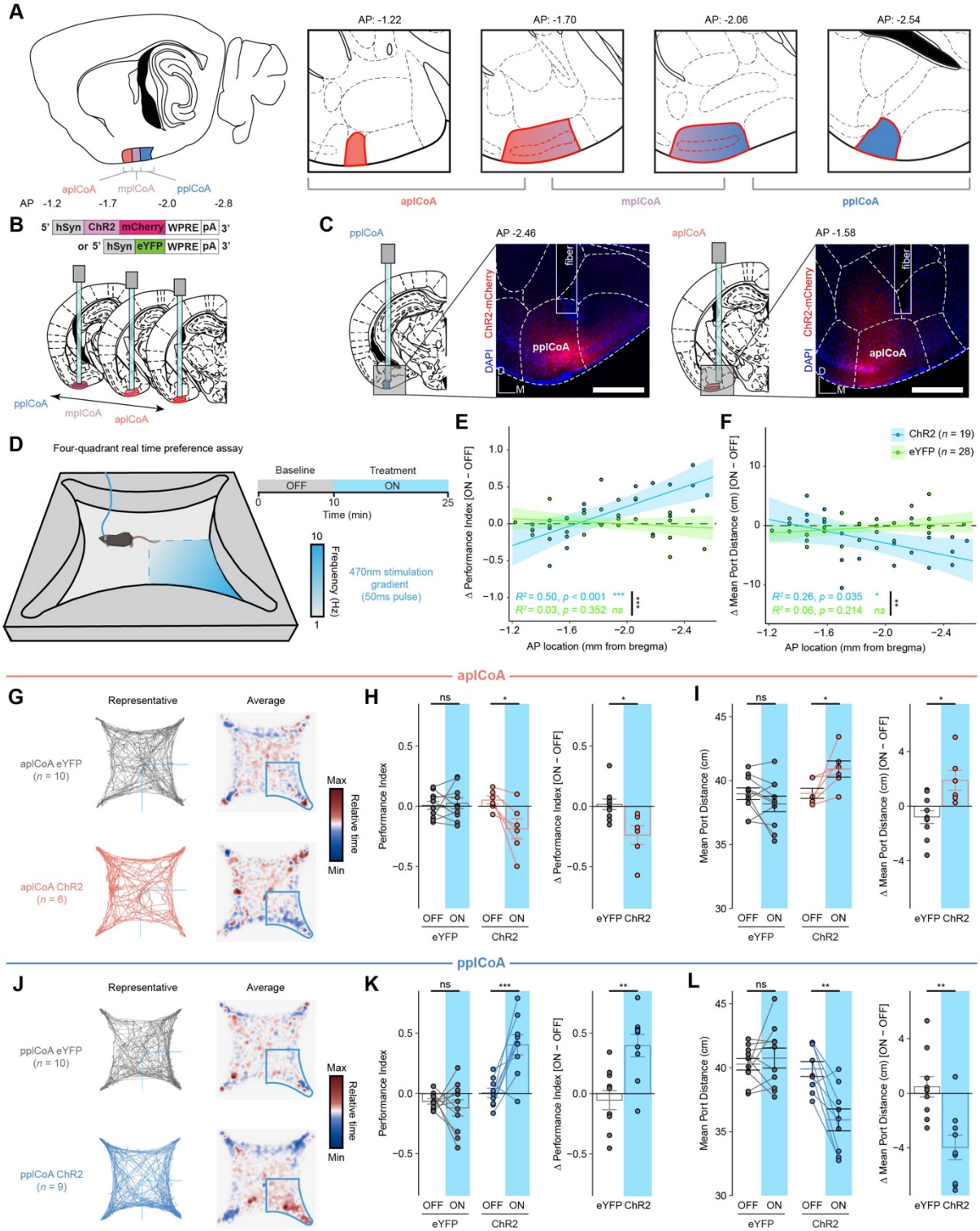
A
AP: -1.22
AP: -1.70
AP: -2.06
AP: -2.54
aplCoA
mplCoA
pplCoA
AP -1.2 -1.7 -2.0 -2.8
B
5' hSyn ChR2 mCherry WPRE pA 3'
or 5' hSyn eYFP WPRE pA 3'
C
pplCoA
AP -2.46
aplCoA
AP -1.58
ChR2-mCherry
DAPI
fiber
D
M
D
Four-quadrant real time preference assay
Baseline
Treatment
OFF
ON
Time (min)
Frequency (Hz)
470nm stimulation gradient (50ms pulse)
E
Δ Performance Index [ON − OFF]
AP location (mm from bregma)
R² = 0.50, p < 0.001 ***
R² = 0.03, p = 0.352 ns
F
ChR2 (n = 19)
eYFP (n = 28)
Δ Mean Port Distance (cm) [ON − OFF]
R² = 0.26, p = 0.035 *
R² = 0.06, p = 0.214 ns
aplCoA
G
Representative
Average
aplCoA eYFP (n = 10)
aplCoA ChR2 (n = 6)
Max
Relative time
Min
H
Performance Index
Δ Performance Index [ON − OFF]
OFF ON
eYFP
ChR2
I
Mean Port Distance (cm)
Δ Mean Port Distance (cm) [ON − OFF]
pplCoA
J
pplCoA eYFP (n = 10)
pplCoA ChR2 (n = 9)
K
L

323

Fig. 2. The plCoA has a topographic organization capable of driving approach and avoidance behaviors.

(A) Schematic of plCoA domains divided into anterior (aplCoA), middle (mplCoA), and posterior (pplCoA) regions based on histology, positioning, and gradients observed in past observations[14].

(B) Strategy to activate anterior-posterior topographical ensembles via optogenetics.

(**C**) Representative histology and fiber/virus placement for aplCoA and pplCoA ChR2 animals.

(**D**) Schematic of four-quadrant open field behavioral assay with closed-loop photostimulation.

(E-F) Linear-fit of change in performance index (**E**) or mean port distance (**F**) as a function of anterior-posterior position along plCoA for optical stimulation.

(G) Paths traveled during the stimulus period for a representative mouse (left) and baseline-normalized collective heatmaps (right) from both the ChR2- and eYFP-infected groups with aplCoA-localized fiber implants. Lower right stimulus quadrant indicated in blue.

(H-I) Mean effect of Photostimulation of aplCoA neurons on time spent in stimulated quadrant (performance index) (**K**) and distance from the corner (port distance) (**I**).

(J) Paths traveled during the treatment period for a representative mouse (left) and baseline-normalized collective heatmaps (right) from both the ChR2- and eYFP-infected groups with pplCoA-localized fiber implants. Lower right stimulus quadrant marked in blue.

(**K-L**) Mean effect of photostimulation of pplCoA neurons infected with ChR2, but not eYFP, is sufficient to increase time spent in the stimulation quadrant (**K**) and reduce its average distance from the stimulation port during the stimulation period (**L**).

Abbreviations: aplCoA, anterior zone of posterolateral cortical amygdala; mplCoA, middle zone of posterolateral cortical amygdala; pplCoA, posterior zone of posterolateral cortical amygdala.

Across panels, ns, not significant; * $p < 0.05$; ** $p < 0.01$; *** $p < 0.001$. Specific details of statistical tests can be found in Supplemental Table 1.

349 TMT is an aversive odor, if posterior plCoA neurons that drive attraction are activated by TMT,
350 then selective activation of this subset without recruiting the full TMT-responsive ensemble
351 should generate an approach response. As established previously, this labeling strategy
352 captures approximately half of Arc-positive neurons (40–100 neurons per 100 μm) [14],
353 leading us to estimate that only a few hundred neurons express ChR2. Mice were then
354 assayed for approach or avoidance behavior during photoactivation of these sparse
355 ensembles (**Figure 2D**). Activation of aplCoA and pplCoA drove avoidance and approach
356 responses, respectively (**Figure S4**). Notably, the magnitude of these behaviors was
357 comparable to that observed during broad activation of each domain (**Figure 2H,K**) and did
358 not differ significantly (**Table S1**). Although it remains possible that behavioral magnitude
359 scales with the number of activated neurons, this question lies beyond the scope of the
360 present study. Nonetheless, these data demonstrate that the opposing behavioral effects of
361 anterior versus posterior plCoA activation are not artifacts of large-scale stimulation.

362 We further examined the effects of anterior-posterior plCoA stimulation on other
363 behaviors to determine whether these effects were specific to appetitive and aversive
364 responses, or if they extended to other affective or motor phenomena. Using the elevated plus
365 maze, we found no change in anxiety based on open arm time or entries, across both the length
366 of plCoA or within either aplCoA or pplCoA (**Figure S5A-C, S5E-F, S5H-I**). In the open field test,
367 we similarly found no changes to thigmotaxis, based on time spent in corners of the open field,
368 or exploration, based on time spent in the center of the open field (**Figure S5K-M, S5O-P, S5R-**
369 **S**). Further, locomotion remained constant during stimulation across both assays and the
370 entirety of plCoA (**Figure S5D, S5G, S5J, S5N, S5Q, S5T**). Together, these data suggest that
371 the effects of plCoA neuron activation across the entire anterior-posterior axis are specific to
372 approach and avoidance, with few other behavioral effects. Overall, we find that activation of
373 plCoA neurons is sufficient to drive behaviors of opposite valence in a topographically organized
374 manner, where aplCoA drives aversion and pplCoA drives attraction.

375 **Molecular Diversity of Transcriptomic plCoA Cell Types Along the Anteroposterior Axis**

376 Having identified a functional axis sufficient to produce approach and avoidance
377 behaviors (**Figure 2**) that does not appear to encode valence (**Figure 1**), we next considered if
378 the plCoA could be topographically organized by molecular cell type to support behaviors of
379 opposing valence. Thus, we sought to determine if there is an axis of molecular cell types along
380 the anteroposterior domains of plCoA. To investigate this phenomenon, we performed single-
381 nucleus RNA sequencing (snRNA-seq) to determine the cell type composition and its
382 relationship to the anterior-posterior axis of plCoA.[37] To simultaneously profile these cell types
383 and identify domain-specific patterns, we separately extracted tissue samples from aplCoA and
384 pplCoA by microdissection, verified accurate dissection by histology, and pooled qualifying
385 samples from the selected plCoA domain for each sequencing run (**Figure 3A, S6A-D**). We also
386 confirmed there were few region- or batch-specific differences in sequencing depth or nuclear
387 quality markers (**Figure S6E-M**). Clustering of sequenced nuclei by gene expression allowed
388 us to initially identify all major canonical neuronal and glial cell types in plCoA based on known
389 marker genes identified in past scRNA-seq studies (**Figure 3B-C**)[27, 28]. Neurons in plCoA are

80% glutamatergic, while 20% of neurons are GABAergic (**Figure 3D**). We also identified large numbers of vascular leptomeningeal cells (VLMCs) and arachnoid barrier cells (ABCs), two fibroblast-like meningeal cell types that interface with vasculature and form a barrier between the brain and CSF, likely due to meningeal presence on the cortical surface during extraction[27-30].

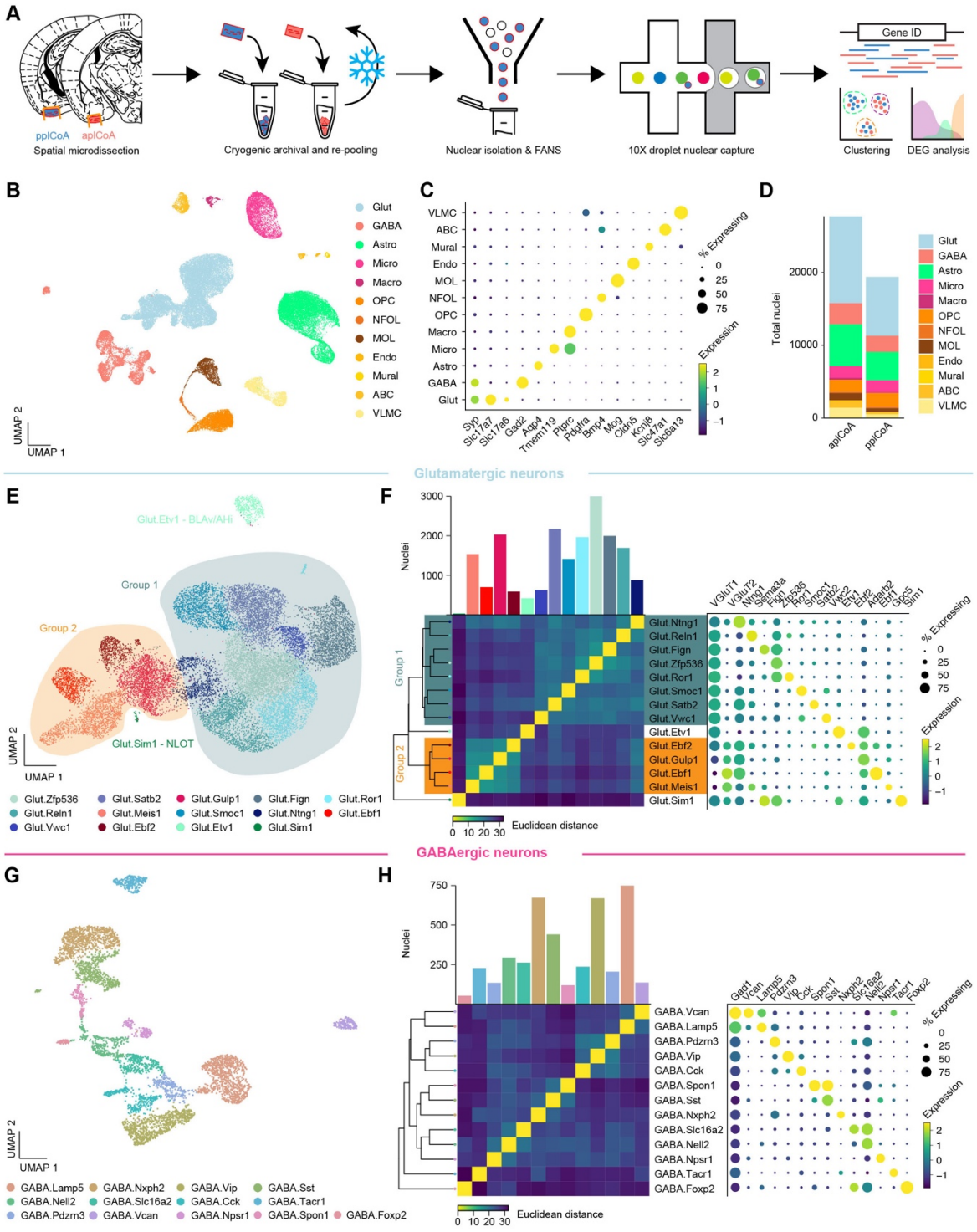

Fig. 3. Transcriptomic heterogeneity of plCoA molecular cell types.
(A) Schematic of freeze and-re-pool strategy for snRNA-seq.
(B) Two-dimensional UMAP (n = 47,132 nuclei, see also **Figure S4.3**), colored by broad cellular identity assigned by graph-based clustering of neuronal and non-neuronal nuclei.
(**C**) Cell-type-specific expression of canonical marker genes indicating broad cellular identity in the brain. Dot size is proportional to percentage of nuclei expressing the marker, with color scale representing normalized expression level.
(**D**) Total proportion of cells of each identified type in each domain of plCoA.
(E) Two-dimensional UMAP of glutamatergic neurons, colored by molecular cell type.
(F) Clustered heatmap showing Euclidean distance between averages of each subtype positioned based on hierarchical clustering (left), and dot plot of marker genes for all glutamatergic subtypes (right).
(G) Two-dimensional UMAP of GABAergic neurons, colored by molecular cell type, like in (**E**).
(H) Clustered heatmap showing Euclidean distance between averages of each subtype positioned based on hierarchical clustering (left), and dot plot of marker genes for all GABAergic subtypes (right), like in (**F**).

412 We further characterized the heterogeneity of glutamatergic and GABAergic neurons
413 within plCoA by re-processing and subclustering both major neuronal cell types. Within
414 glutamatergic neurons, we identified 14 distinct subtypes by gene expression, with largely
415 continuous variation between glutamatergic subtypes (**Figure 3E**). However, when examining
416 the relationships between these subtypes, we identified two broader groups of glutamatergic
417 neurons via hierarchical clustering, where subtypes within each group displayed a lower
418 Euclidean distance from one another in high-dimensional gene expression space (**Figure 3F**).
419 Each of these two broader groups had a marker for every type within either group, where the
420 larger Group 1 of glutamatergic neurons express *Slc17a7 (VGLUT1)*, and the smaller Group 2
421 expresses *Slc17a6 (VGLUT2)*. Within each of these glutamatergic groups, most observed
422 marker genes are non-canonical in the amygdala and cortex, suggesting unique glutamatergic
423 ensembles or patterns of gene expression within glutamatergic neurons in plCoA compared to
424 other regions previously described. Two subtypes did fall outside of either broad glutamatergic
425 group, varying in a more discrete manner than most plCoA glutamatergic neuron subtypes.
426 Interestingly, examination of data from the Allen ISH Atlas for their respective marker genes
427 *Etv1* and *Sim1* showed these two groups fall into adjacent regions outside of plCoA, where
428 Glut.Etv1 neurons localize to the posterior basomedial amygdala and Glut.Sim1 neurons
429 localize to the nucleus of the lateral olfactory tract (**Figure S7A-B**). However, gene expression
430 patterns for GABAergic neurons displayed an opposing form of heterogeneity, where subtypes
431 are more discrete, without broad groups linking related subtypes (**Figure 3G**). Marker genes for
432 GABAergic neurons are also more canonical than those in glutamatergic neurons, whereby
433 most GABAergic neurons in plCoA have interneuron-like identities, expressing canonical marker
434 genes such as *Vip, Sst,* and *Cck* (**Figure 3H**).

435 We hypothesized that differences in these populations' abundance could potentially be
436 responsible for the difference observed between different plCoA domains, and thus examined
437 potential domain-specific enrichment of certain cell types within plCoA. Visualization of these
438 nuclei with UMAP showed little clear region-specific structure for any major cell types (**Figure**
439 **4A**). This lack of structure was broadly confirmed quantitatively, where a few low-abundance
440 glial cell types showed significant domain-specific enrichment, but the high-abundance major
441 cell types did not (**Figure 4A-B**). In other brain areas, variations in the characteristics of
442 subgroups within major cell types are more pronounced than variations in the total numbers of
443 these major cell types, i.e. the balance of genes rather than balance of subtypes[31, 32].
444 Therefore, we examined abundance of differentially expressed genes (DEGs) between plCoA
445 domains for each major cell type. Here, we found that both major neuronal cell types had more
446 abundant DEGs than all major glial cell types (**Figure 4C**). Glutamatergic neurons DEGs
447 exceeded all other major cell types by a factor of 4, suggesting that differences between the
448 anterior and posterior domains are most likely to be observed via variation in glutamatergic
449 neurons.

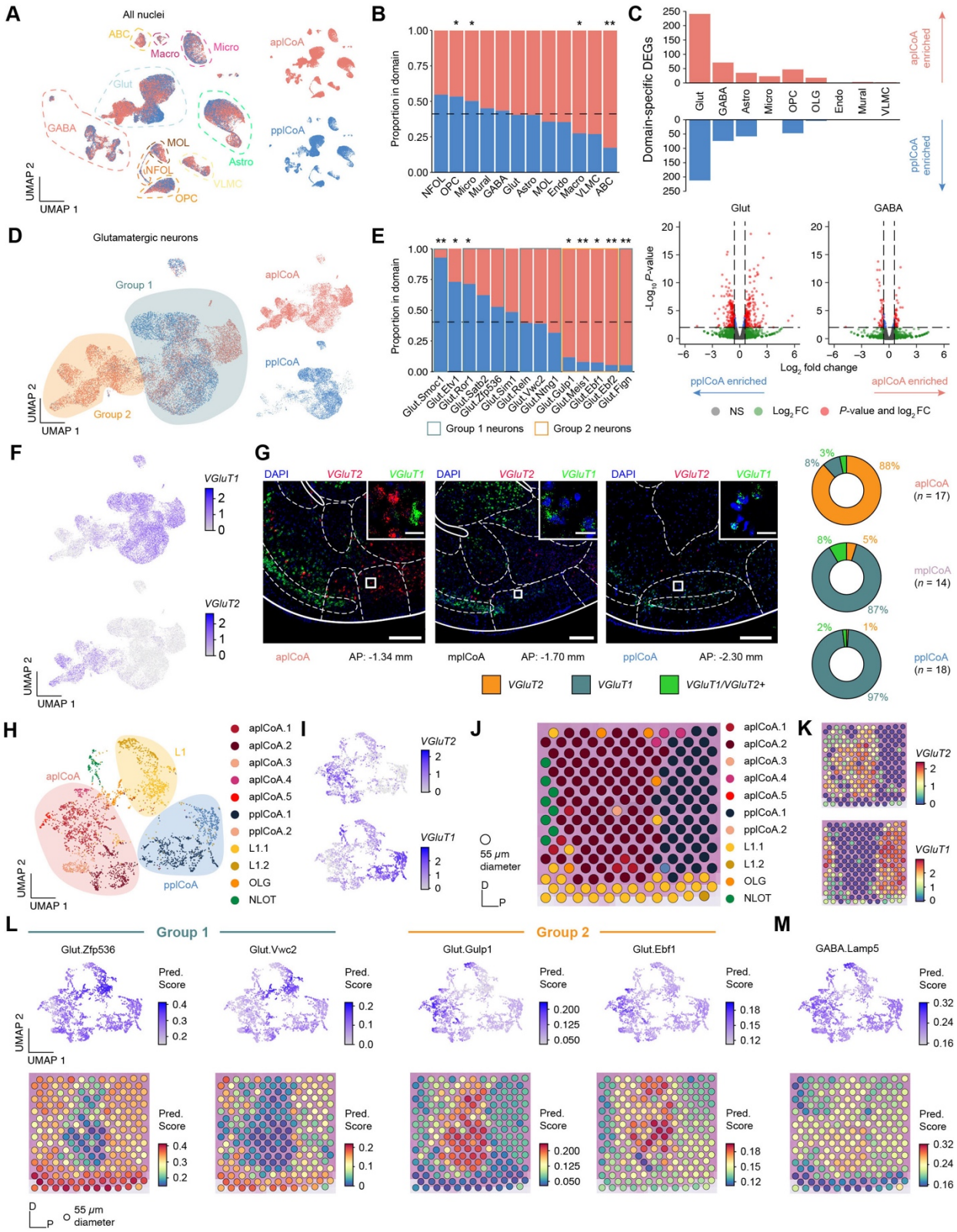
A
All nuclei
ABC
Macro
Micro
Glut
GABA
MOL
NFOL
OPC
VLMC
Astro
aplCoA
pplCoA
UMAP 2
UMAP 1
B
Proportion in domain
NFOL OPC Micro Mural GABA Glut Astro MOL Endo Macro VLMC ABC
C
Domain-specific DEGs
Glut GABA Astro Micro OPC OLG Endo Mural VLMC
aplCoA enriched
pplCoA enriched
D
Glutamatergic neurons
Group 1
Group 2
E
Glut.Smoc1 Glut.Etv1 Glut.Ror1 Glut.Satb2 Glut.Zfp536 Glut.Sim1 Glut.Reln Glut.Vwc2 Glut.Nthng1 Glut.Gulp1 Glut.Meis1 Glut.Ebf1 Glut.Ebf2 Glut.Fign
Group 1 neurons
Group 2 neurons
Glut
GABA
-Log10 P-value
Log2 fold change
pplCoA enriched
aplCoA enriched
NS
Log2 FC
P-value and log2 FC
F
VGluT1
VGluT2
G
DAPI
VGluT2
VGluT1
aplCoA
AP: -1.34 mm
mplCoA
AP: -1.70 mm
pplCoA
AP: -2.30 mm
VGluT2
VGluT1
VGluT1/VGluT2+
aplCoA (n = 17)
mplCoA (n = 14)
pplCoA (n = 18)
H
aplCoA.1
aplCoA.2
aplCoA.3
aplCoA.4
aplCoA.5
pplCoA.1
pplCoA.2
L1.1
L1.2
OLG
NLOT
L1
aplCoA
pplCoA
I
J
55 μm diameter
K
L
Group 1
Group 2
Glut.Zfp536
Glut.Vwc2
Glut.Gulp1
Glut.Ebf1
Pred. Score
M
GABA.Lamp5

450

Fig. 4. Glutamatergic neurons subtypes in plCoA are spatially distributed along an anteroposterior molecular gradient.

(**A**) UMAP of all plCoA nuclei colored by zone of origin, with dotted outlines and labels denoting the major cell types.

(**B**) Relative proportion of nuclei from each domain within each broad identity class. Dotted line indicates chance level for all plCoA nuclei.

(**C**) Top, abundance of domain-specific DEGs for each major cell type, either enriched in aplCoA nuclei (top) or pplCoA nuclei (bottom). Bottom, volcano plots for domain-specific DEGs for glutamatergic (left) and GABAergic neurons (right), the two cell types with the greatest degree of domain specific gene expression, where negative log-fold changes indicate enrichment in pplCoA and positive log-fold changes indicate enrichment in aplCoA.

(**D**) UMAP of plCoA glutamatergic neurons colored by domain of origin, with dotted outlines and labels denoting the subtypes on the graph. Groups of glutamatergic neuron types identified previously via Euclidean distance and hierarchical clustering are overlaid on top of the neuron types of interest.

(**E**) Relative proportion of molecular subtypes from each domain within glutamatergic neurons, where relevant subtypes are outlined according to their glutamatergic neuron group. Dotted line indicates chance level for plCoA glutamatergic neuron nuclei.

(**F**) UMAP of all glutamatergic neuron nuclei, colored by expression levels of *VGluT2* (top) or *VGluT1* (bottom).

(**G**) Left, representative images of *in situ* RNAscope labeling of *VGluT2* RNA (red) and *VGluT1* RNA (green) across plCoA domains. Right, proportions of glutamatergic neurons expressing *VGluT2, VGluT1,* or both. Scale bars, 500 μm (main image), 50 μm (inset).

(**H**) UMAP of all plCoA-overlapping Visium capture spots, colored by cluster. Broad spatial position of groups of clusters are overlaid on top of the capture spots of interest.

(**I**) UMAP of all plCoA-overlapping Visium capture spots, colored by expression levels of *VGluT2* (top) or *VGluT1* (bottom).

(**J**) Representative plCoA-overlapping region of one section on a Visium slide capture area, with capture spots colored by cluster.

(**K**) Representative plCoA-overlapping region of one section on a Visium slide capture area, with capture spots colored by expression levels of *VGluT2* (top) or *VGluT1* (bottom).

(**L**) Prediction scores for representative glutamatergic neuron subtypes within Group 1 (left) and Group 2 (right), shown on a UMAP of all plCoA-overlapping capture spots across all sections (top) and on a representative plCoA-overlapping region of one section (bottom).

(**M**) Prediction scores for a representative GABAergic neuron subtype, shown on a UMAP of all plCoA-overlapping capture spots across all sections (top) and on a representative plCoA-overlapping region of one section (bottom).

Across panels: * $p < 0.05$; ** $p < 0.01$; *** $p < 0.001$; ns, not significant. Additional specific details of statistical tests can be found in Supplemental Table 1.

491
492 Upon examination of domain-specific variation in plCoA glutamatergic neurons, we
493 initially observed a greater degree of domain-specific clustering in dimension-reduced space
494 (**Figure 4D**). Glutamatergic neuron subtypes correspondingly displayed domain-specific
495 enrichment, where more than half of glutamatergic neuron subtypes were significantly enriched
496 in either the anterior or posterior plCoA domain (**Figure 4E**). Upon closer examination, we found
497 that every glutamatergic subtype in the *VGluT2*-expressing Group 1 was enriched in anterior
498 plCoA, while *VGluT1*-expressing Group 2 subtypes are evenly distributed across fields or
499 biased towards the posterior, with one exception, Glut.Fign, which likely derives from the
500 aplCoA-adjacent cortex-amygdala transition area CxA, based on Allen ISH data of *Fign*
501 expression (**Figures 4F, S7A**). In contrast to glutamatergic neurons, we did not observe
502 significant plCoA domain-specific variation for any GABAergic neuron subtypes (**Figure S7D-E**).
503 We also found additional heterogeneity within glial cell types, including additional subtypes
504 within astrocytes and VLMCs (**Figure S7G-J, O-R**). We also observed domain-specific
505 divergence in gene expression for OPCs and astrocytes corresponding to domain-specific DEG
506 differences, though they did not correspond to any observable differences in subtype
507 enrichment (**Figure S7F, K-N**).

508 To confirm these findings and validate our snRNA-seq data, we directly examined spatial
509 RNA expression patterns. First, we used RNAscope labelling to examine the expression of
510 *VGluT2* and *VGluT1 in situ* in the plCoA, quantifying the number of nuclei expressing these
511 genes. We found that anterior plCoA had a much greater proportion of RNAscope-labelled
512 *VGluT*2+ nuclei (88%) than *VGluT*1+ nuclei (11%) compared to the rest of plCoA, where
513 *VGluT*1+ neurons predominate; posterior plCoA nuclei were almost entirely *VGluT1*+ (97%)
514 expressing (**Figure 4G**). It is noteworthy that these numbers were generally consistent with
515 those in our sequencing data.

516 The RNAscope patterns provide cellular resolution for two broadly distinct groups, but
517 lacks information on the broad distribution of more nuanced subtypes along the AP axis. Thus,
518 we next analyzed spatial gene expression in the plCoA from an existing Visium spatial
519 transcriptomics dataset that contained sagittal sections bisecting the plCoA along the midline
520 (Romero et al., in preparation; **Figure S7S**). Although the spatial resolution is limited to 55 μm
521 spots, this data set afforded an opportunity to test if the cell types we had identified by snRNA-
522 seq were distributed in a spatial gradient along the plCoA axis. We asked if the domain-specific
523 molecular cell type composition can be recovered directly from spatial information, without
524 depending on inference from dissection histology. All sections used were of similarly high quality
525 and did not display any clearly observable batch effects, with all but one having more than 100
526 spots covering the plCoA (**Figure S7T-W**). When clustering directly on spatial data, we
527 observed significant heterogeneity separating into three broad groups (**Figure 4H**). Like in
528 scRNA-seq, we found highly specific expression of *VGluT2* and *VGluT*1 to two of the three
529 broad spot groups (**Figure 4I**). When examining the spatial configuration of these groups, we
530 found the *VGluT*2-expressing group of clusters was in aplCoA, while the *VGluT*1-expressing
531 group was in pplCoA**,** with the third intermediate group corresponding to layer 1 (**Figure 4J-K**).
532 When computationally projecting transcriptomic cell type identities onto spatial data, we
533 observed that Group 1 glutamatergic neuron types would project onto pplCoA spots and Group

534 2 glutamatergic neuron types would project onto aplCoA spots, while negligible anteroposterior
535 bias could be observed when projecting GABAergic neuron types onto plCoA spots (**Figure 4L-**
536 **M**). It is important to note that this data set was collected from non-transgenic litter mate
537 controls in a study of APP23 Alzheimer's model. The mice were of the same genetic
538 background (C57BL/6J) but a different age as our sequencing specimens. Thus, these data
539 confirm the robustness of our findings from sn-RNA-seq and in situ hybridization, and further
540 demonstrate that plCoA contains a diverse population of numerous neuronal subtypes that vary
541 along a gradient. Whereas glutamatergic neuron subtypes vary significantly along the
542 anteroposterior axis, such that aplCoA-enriched subtypes express *VGluT*2 and pplCoA-enriched
543 subtypes express *VGluT1.*

544 **Molecularly Defined plCoA Glutamatergic Neuron Populations Contribute to Approach**
545 **and Avoidance Behaviors**

546 Given this spatial distribution bias of plCoA$^{VGluT2+}$ neurons into aplCoA and plCoA$^{VGluT1+}$
547 neurons into pplCoA, we further hypothesized that these glutamatergic neuron subtypes could
548 be responsible for the opposing valence responses observed during topographic plCoA
549 stimulation (**Figure 2**). We reasoned that if distinct molecular cell types mediate opposing
550 valence, then activation of them in a topography-independent manner should elicit opposing
551 responses. Therefore, we expressed ChR2 in a non-spatially-biased, cell type-specific manner
552 using a Cre-dependent viral construct in *VGluT2::Cre* and *VGluT1::Cre* transgenic mice,
553 targeting AAV-DIO-hSyn-ChR2 into mplCoA and implanting optic fibers above the injection site
554 (**Figures 5A-B, S3B**). Using the prior four-quadrant open field task, we found that
555 photostimulation of plCoA$^{VGluT2+}$ neurons significantly reduced time spent in the 'on' quadrant
556 and increased the average distance to the corner port during the treatment period, indicating
557 that activation of plCoA$^{VGluT2+}$ neurons is aversive and leads to avoidance of the quadrant when
558 paired with stimulation (**Figure 5C-E**). In contrast, photostimulation of the plCoA$^{VGluT1+}$ neurons
559 instead increased the time in the 'on' quadrant and decreased average distance to the corner
560 port, indicating plCoA$^{VGluT1+}$ neuron activation is appetitive and leads to attraction to the
561 stimulation quadrant (**Figure 5C,F-G**). These data suggest that the divergent domain-specific
562 valence effects of plCoA activity could be due to the divergent molecularly defined neuronal
563 ensembles predominant in each topographical field of plCoA.

564 Next, we sought to determine whether these two glutamatergic populations are
565 respectively required for innate attraction and aversion to odor. We used the above transgenic
566 mouse lines to drive expression of a viral Cre-dependent hM4D(Gi) construct to selectively
567 inhibit these neurons' activity via chemogenetics [33] (**Figure 5I, Figure S7).** We administered
568 clozapine-N-oxide (CNO) or a vehicle control and used the four-quadrant open field assay[14] to
569 assess their behavioral responses to the innately-attractive 2PE or the innately-aversive TMT to
570 determine the difference in the magnitude of temporally-counterbalanced valence responses
571 when the respective populations are chemogenetically silenced. These two odors were chosen
572 because they most robustly drive approach and avoidance, and were used in our previous work
573 demonstrating the role of plCoA in innate responses[14].

574

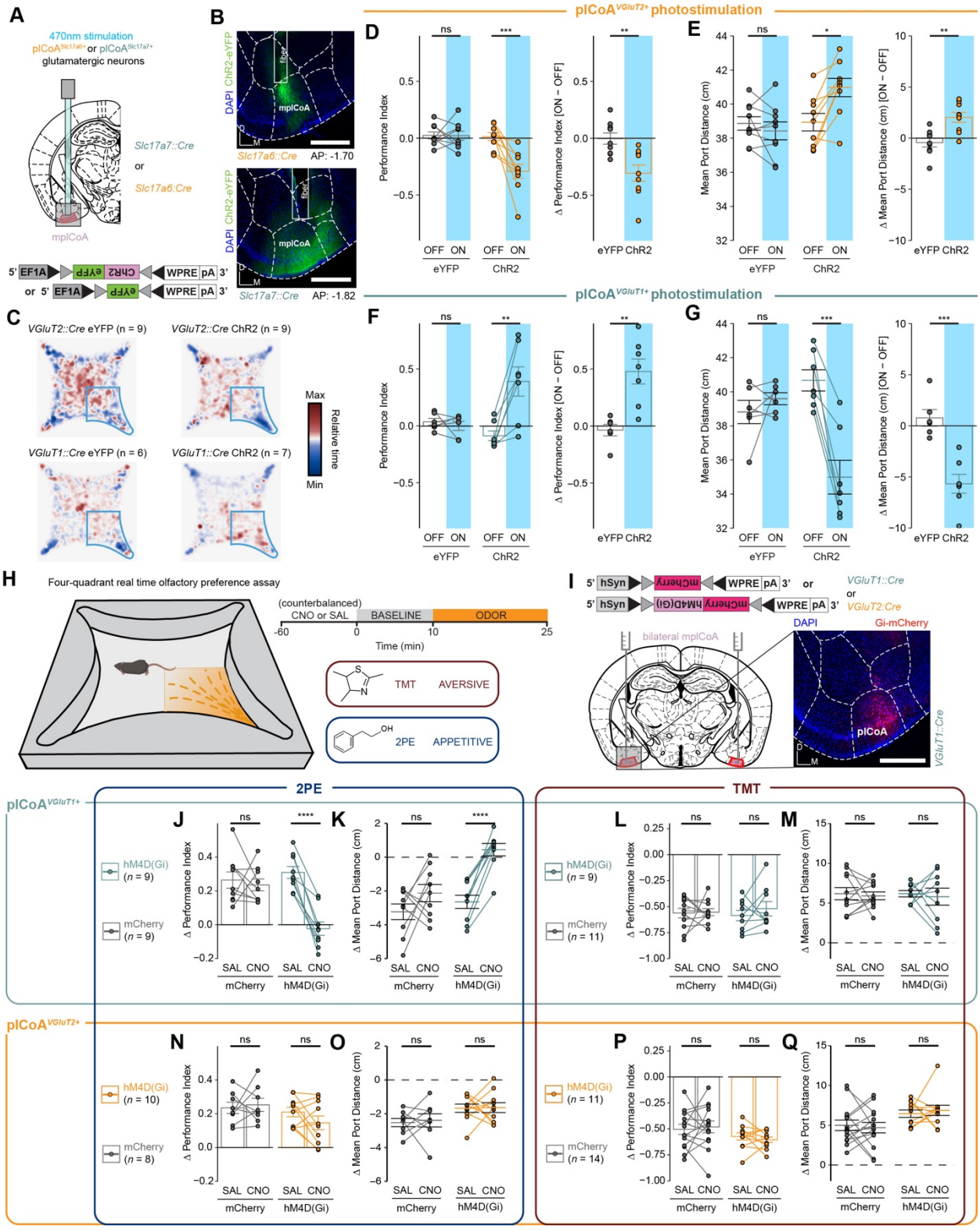
A
470nm stimulation
pICoA Slc17a6+ or pICoA Slc17a7+
glutamatergic neurons
Slc17a7::Cre
or
Slc17a6:Cre
mpICoA
5' EF1A eYFP ChR2 WPRE pA 3'
or 5' EF1A eYFP WPRE pA 3'
B
DAPI ChR2-eYFP
fiber
mpICoA
Slc17a6::Cre AP: -1.70
Slc17a7::Cre AP: -1.82
pICoA VGluT2+ photostimulation
D
E
Performance Index
Δ Performance Index [ON – OFF]
Mean Port Distance (cm)
Δ Mean Port Distance (cm) [ON – OFF]
OFF ON
eYFP
ChR2
pICoA VGluT1+ photostimulation
F
G
C
VGluT2::Cre eYFP (n = 9)
VGluT2::Cre ChR2 (n = 9)
VGluT1::Cre eYFP (n = 6)
VGluT1::Cre ChR2 (n = 7)
Max
Relative time
Min
H
Four-quadrant real time olfactory preference assay
(counterbalanced)
CNO or SAL
BASELINE
ODOR
-60 0 10 25
Time (min)
TMT AVERSIVE
2PE APPETITIVE
I
5' hSyn mCherry WPRE pA 3'
or
5' hSyn mCherry hM4D(Gi) WPRE pA 3'
VGluT1::Cre
or
VGluT2::Cre
bilateral mpICoA
DAPI
Gi-mCherry
pICoA
VGluT1::Cre
2PE
TMT
pICoA VGluT1+
J
K
L
M
hM4D(Gi) (n = 9)
mCherry (n = 9)
mCherry (n = 11)
Δ Performance Index
Δ Mean Port Distance (cm)
SAL CNO
mCherry
hM4D(Gi)
pICoA VGluT2+
N
O
P
Q
hM4D(Gi) (n = 10)
mCherry (n = 8)
hM4D(Gi) (n = 11)
mCherry (n = 14)

575

576 **Fig. 5. Glutamatergic plCoA$^{VGluT2+}$ and plCoA$^{VGluT1+}$ neurons contribute to innate approach**
577 **and avoidance behaviors.**
578 (**A**) Schematic for selective photostimulation of distinct glutamatergic cell type. *VGluT2::Cre* and
579 *VGluT1::Cre* animals were injected with Cre-dependent viral vectors into mplCoA with a fiber
580 optic implant placed just above the injection site.
581 (**B**) Representative histology from ChR2 viral injection and fiber implantation site in an
582 *VGluT2::Cre* animal (top) and an *VGluT1::Cre* animal (bottom).
583 (**C**) Baseline-normalized collective heatmaps from both the ChR2- and eYFP-infected groups in
584 *VGluT2::Cre* and *VGluT1::Cre* animals with plCoA-localized fiber implants. Lower right stimulus
585 quadrant marked in blue.
586 **(D-G)** Effect of photostimulation of plCoA$^{VGluT2+}$ neurons (**D-E**) or plCoA$^{VGluT1+}$ neurons (**F-G**) on
587 time spent in the stimulation quadrant (**D, F**) and distance from the corner (**E, G**).
588 (**H**) Behavioral paradigm to assess innate valence responses to odor. Left, schematic of four-
589 quadrant open field behavioral assay for spatially-specific odor delivery. Upper right, within-trial
590 timeline. Lower right, odors delivered and their associated innate valence.[3]
591 (**I**) Schematic of strategy for selective chemoinhibition of molecularly defined glutamatergic
592 plCoA neurons.
593 (**J-M**) Effect of chemoinhibition of plCoA $^{VGluT1+}$ neurons on time spent in the odor quadrant (**J, L)**
594 or decrease in mean port distance (**K, M**) in response to 2PE (**J-K**) or TMT (**L-M**).
595 (**N-Q**) Effect of chemoinhibition of plCoA $^{VGluT2+}$ neurons on time spent in the odor quadrant (**N,**
596 **P)** or decrease in mean port distance (**O, Q**) in response to 2PE (**N-O**) or TMT (**P-Q**).
597 Across panels, ns, not significant; * $p < 0.05$; ** $p < 0.01$; *** $p < 0.001$, **** $p < 0.0001$.
598 Additional specific details of statistical tests can be found in Supplemental Table 1.

599 We observed that both transgenic mouse lines displayed attraction and aversion to 2PE
600 and TMT following administration of the vehicle control. Inhibiting plCoA$^{VGluT2+}$ neurons by CNO
601 administration did not affect the response to either odorant (**Figure 5J-Q**). However, inhibiting
602 plCoA$^{VGluT1+}$ neurons abolished the attraction to 2PE, without affecting aversion to TMT (**Figure**
603 **5J-Q**). In other words, neither group of plCoA glutamatergic neurons are selectively required for
604 TMT aversion, but plCoA$^{VGluT1+}$ neurons are required for attraction to 2PE. Further, silencing of
605 either population did not lead to any broader non-olfactory behavior effects as measured by the
606 EPM and OFT assays, including anxiety, exploration, and motility, showing the effects of
607 silencing these neurons are likely limited to valence and/or olfaction alone, instead of
608 exploratory or defensive behaviors (**Figure S8C-N**). The necessity of plCoA$^{VGluT1+}$ neurons for
609 2PE attraction, combined with their ability to drive approach responses with stimulation indicates
610 that these of plCoA$^{VGluT1+}$ neurons signal attraction. However, plCoA$^{VGluT2+}$ neurons, although
611 sufficient to drive aversion, are not necessary for aversion. Further work is required to better
612 identify a molecularly defined population necessary for aversive responses.

613 **A Topographic Organization of plCoA Defined by Limbic Projection Targets**

614 The anatomical connectivity of the plCoA has not yet been defined in the mouse brain.
615 Further, we posited that the differences in necessity of plCoA cell types could be due to
616 divergent downstream connections instead of divergent molecular features, which may partially,
617 but not completely overlap. Thus, we next sought to identify distinct downstream outputs of
618 plCoA that could explain the bidirectional valence effects of its topography. We first
619 characterized the downstream outputs of plCoA by co-injecting the anterograde viral tracer
620 AAV-DIO-hSyn-mRuby2-T2A-synaptophysin-EGFP and a constitutive AAV-Cre virus into
621 mplCoA to label presynaptic terminals with EGFP (**Figure S9A-B**). We observed a high amount
622 of terminal fluorescence within plCoA itself, suggesting the presence of recurrent connections
623 within the region (**Figure S8B**). In addition, we observed long-range projections to a diverse set
624 of regions, including surrounding extended amygdala subregions, such as MeA and the
625 amygdalo-hippocampal transition area (AHi), regions controlling valence and emotion, like the
626 NAc and the bed nucleus of the stria terminalis (BNST), and regions involved in olfactory
627 processing, primarily PIR and OT (**Figure 6A-D**). The projection to the NAc is broad without any
628 apparent spatial restriction, innervating both the core and shell.

629 Among these outputs, we hypothesized that the NAc and the MeA could be responsible
630 for the behavioral divergence between anterior and posterior plCoA, given their known
631 involvement in reward expectation and aversion, respectively[34, 35]. We sought to confirm
632 these differences using retrograde tracing from MeA or NAc, where red retrobeads were
633 injected into MeA or NAc and labeled neurons were quantified along the anterior-posterior axis
634 (**Figure 6E**). For both downstream targets, we observed opposing gradients of retrobead
635 projector labeling throughout the entire plCoA anteroposterior axis (**Figure 6F**). MeA-projecting
636 neurons are enriched in aplCoA, and NAc-projecting neurons are enriched in pplCoA, with each
637 having a frequency of around chance level in mplCoA (**Figure 6G**). Further, the majority of
638 labeled plCoA-MeA projection neurons were in aplCoA, while the majority of labeled plCoA-NAc
639 projection neurons were in pplCoA (**Figure 6H**). To further confirm the spatial bias in projection
640 targets, we performed anterograde tracing from the aplCoA and pplCoA by injecting viruses

expressing either eYFP or mCherry into either domain of plCoA in a counterbalanced manner (**Figure S9D-E**). Anterograde projection strength from aplCoA and pplCoA revealed that projections to MeA were most dense from aplCoA, and projections to NAc were most dense from pplCoA (**Figure 6I-K**). The aplCoA sent a significantly higher proportion of its projections to MeA than pplCoA, whereas pplCoA sent a significantly higher proportion of its projections to NAc (**Figure 6L**).

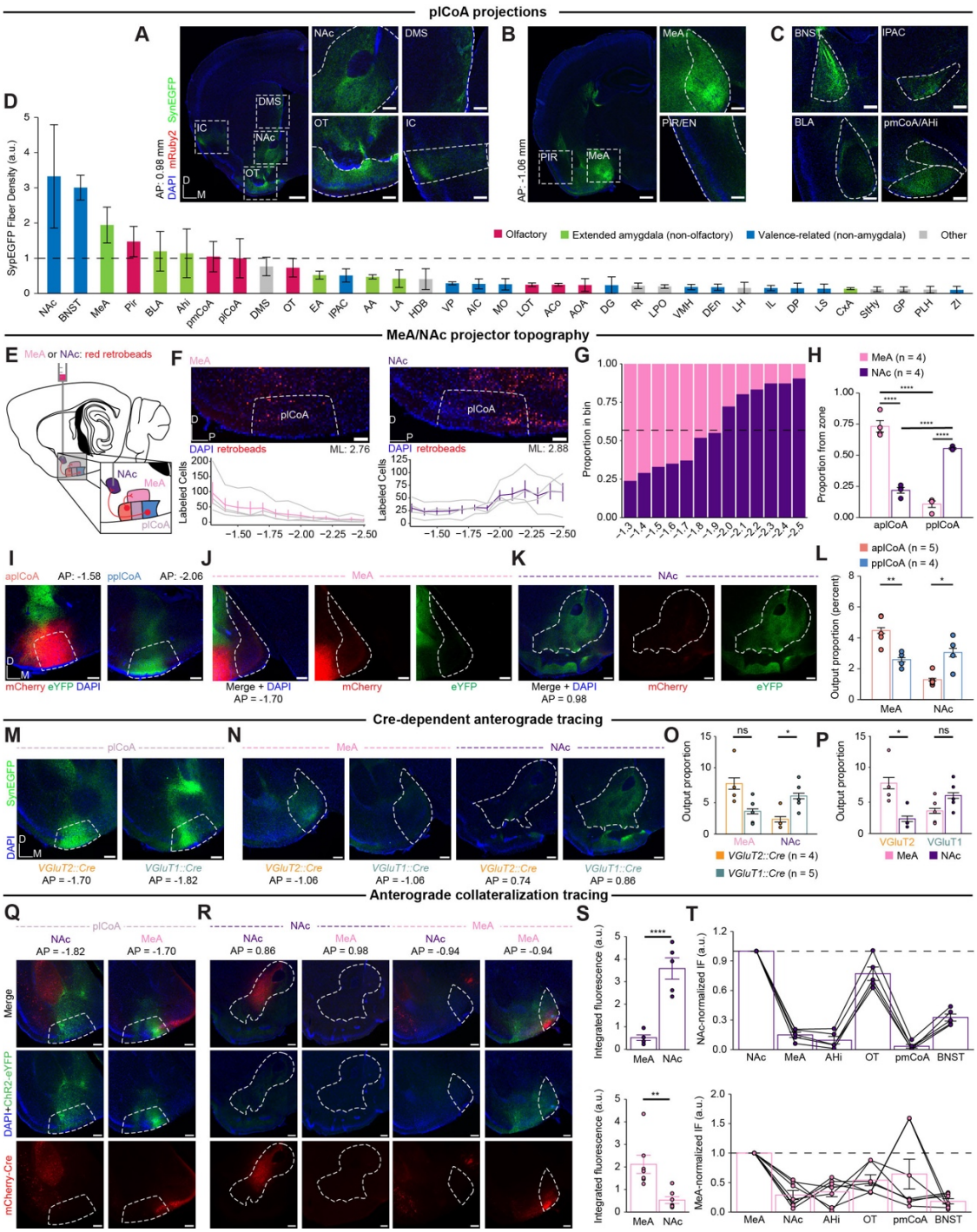

Fig. 6. Projections to MeA and NAc from plCoA are Topographically Organized

(**A**) Left, whole-hemisphere view at AP = 0.98 mm from bregma. Scale bar, 500 µm. Right, Magnified images of the areas highlighted inside white dashed lines. Scale bar, 200 µm.

(**B**) Left, whole-hemisphere view at AP = -1.06 mm from bregma. Scale bar, 500 µm. Right, Magnified images of the areas highlighted inside white dashed lines. Scale bar, 200 µm.

(**C**) Other plCoA projections not found in cross-sections of the brain found in **(A)** and **(B)**. Scale bar, 200 µm.

(**D**) Magnitude of anterograde synaptophysin-eYFP fluorescence in primary downstream targets of plCoA projection neurons ordered by total output strength, colored based on each region's function.

(**E**) Schematic for topographic retrograde mapping strategy from MeA and NAc into plCoA. Red retrobeads are injected into MeA or NAc and topographical projection bias is examined along the anterior-posterior axis.

(**F**) Representative images (top) for injection into MeA (left) or NAc (right) and number of neurons labeled along the anterior-posterior axis as distance (mm) from bregma (bottom). Gray lines denote individual replicates, where colored lines indicate mean ± s.e.m.

(**G**) Proportion of retrobead-labeled neurons projecting to MeA or NAc for each 100 µm segment as a function of distance from bregma. Dashed line indicates overall balance of all retrobead-labeled neurons across entire plCoA.

(**H**) Proportion of retrobead-labeled neurons from either target within each plCoA zone. MeA-labeled neurons are significantly enriched in aplCoA compared to NAc-labeled neurons, while NAc-labeled neurons are significantly enriched in pplCoA compared to those labeled from MeA.

(**I**) Representative histological images for the injection sites in aplCoA (left) and pplCoA (right) from a representative animal. Scale bar, 200 µm.

(**J**) Representative histological images for MeA from the animal in (**J**). Scale bar, 200 µm.

(**K**)**.** Representative histological images for NAc from the animal in (**J**). Scale bar, 200 µm.

(**L**) Output strength as a proportion of total fluorescence from aplCoA and pplCoA to MeA and NAc.

(**M**) Representative histological images for the injection site in plCoA from a representative *VGluT1::Cre* and *VGluT2::Cre* animal. Scale bar, 200 µm.

(**N**) Representative histological images from MeA and NAc from a representative animal of either genotype. Scale bar, 200 µm.

(**O**) Left, output strength as a proportion of total fluorescence from plCoA$^{VGluT2+}$ and plCoA$^{VGluT1+}$ neurons to MeA and NAc. Right, comparison of same data, but by target region within genotype.

(**P**) Same data as **(O)**, but by target region within genotype.

(**Q-T**) Mapping collateral projections from NAc- and MeA projecting neurons.

(**Q**) Representative histological images for the injection site in plCoA from a representative animal receiving retrograde virus into MeA or NAc. Scale bar, 200 µm.

(**R**) Representative histological images of NAc and MeA retro-Cre targeting (red) and outputs (green).

(**S**) Comparison of absolute integrated fluorescence intensities in MeA and NAc when retroAAV was injected into NAc (top) or MeA (bottom).

(**T**) Quantification of fluorescence in selected downstream brain regions from plCoA originating from plCoA-NAc neurons proportional to eYFP fluorescence in NAc (top) or MeA (bottom).

692 Abbreviations: NAc, nucleus accumbens; BNST, bed nucleus of stria terminalis; MeA, medial
693 amygdala; Pir, piriform cortex; BLA, basolateral amygdala; Ahi, amygdalo-hippocampal
694 transition area; pmCoA, posteromedial cortical amygdala; Str, striatum; OT, olfactory tubercle;
695 EA, extended amygdala; IPAC, inferior peduncle of the anterior commissure; AA, anterior
696 amygdala; LA, lateral amygdala; HDB, horizontal limb of the diagonal band; VP, ventral
697 pallidum; AIC, anterior insular cortex; mfb, medial forebrain bundle; MO, medial orbitofrontal
698 cortex; LOT, lateral olfactory tract; ACo, anterior cortical amygdala; AOA, anterior olfactory area;
699 DG, dentate gyrus; Rt, reticular nucleus; LPO, lateral preoptic area; VMH, ventromedial
700 hypothalamus; DEn, dorsal endopiriform claustrum; LH, lateral hypothalamus; IL, infralimbic
701 cortex; DP, dorsal peduncular cortex; LS, lateral septum; CxA, cortex-amygdala transition area;
702 sox, supraoptic decussation; StHy, striohypothalamic nucleus; GP, globus pallidus; PLH,
703 perirhinal cortex; ZI, zona incerta.
704 Across panels, ns, not significant; * $p < 0.05$; ** $p < 0.01$; **** $p < 0.0001$. Additional specific
705 details of statistical tests can be found in Supplemental Table 1.

706 We reasoned that the topographical sufficiency we observed (**Figure 2**) could be
707 explained by cell type-specific divergence in projection target, whereby the topographical biases
708 in downstream targets are recapitulated by their underlying molecular cell type. To determine
709 the relationship between cell types and projection targets, we injected Cre-dependent eYFP into
710 mplCoA in *VGluT2::Cre* and *VGluT1::Cre* transgenic mice, targeting the middle to ensure
711 differences result from cell type, instead of simply redundant topography (**Figure S9F-G)**.
712 Interestingly, the relationship was not as simple as one cell type, one primary projection target.
713 Rather, both cell types project to both structures in different proportions. The plCoA$^{VGluT2+}$
714 neurons primarily project to MeA with a significant bias for that target over NAc, while
715 plCoA$^{VGluT1+}$ neurons project to both MeA and NAc, with a statistically insignificant bias toward
716 NAc (**Figure 6M,P**). These findings demonstrate that NAc primarily receives projections from
717 plCoA$^{VGluT1+}$ neurons, whereas the MeA receives input from both populations. Moreover,
718 projection of both cell types to the MeA may explain why neither *VGluT* population was
719 selectively required for innate aversion (**Figure 5J-Q**).

720 We further characterized *VGluT* expression in projection-defined neurons by combining
721 retrograde tracing from either the MeA or NAc with *in situ* RNAscope for *VGluT1* and *VGluT2*
722 (**Figure S10**). Given that the anterior and posterior regions of plCoA are predominately *VGluT2*
723 and *VGluT1* positive (**Figure 4G**), respectively, and both regions send projections to the MeA
724 and NAc (**Figure 6M-P**), we focused our analysis on the middle plCoA, which contains a more
725 balanced mixture of these cell types. In this region, we found that most MeA-projecting neurons
726 (62%) expressed *VGluT2*, whereas only a small fraction (4%) expressed *VGluT1*. In contrast,
727 NAc-projecting neurons were largely VGluT1-positive (64%), with an additional 20% co-
728 expressing both *VGluT1* and *VGluT2*. A subset of retrogradely labeled neurons appeared
729 negative for both markers, which may reflect detection limits or the presence of non-
730 glutamatergic projection neurons. Overall, these results align with the anterograde tracing data,
731 indicating that *VGluT2*-expressing neurons predominantly project to the MeA, *VGluT1*-
732 expressing neurons primarily project to the NAc, and a smaller population projects to both
733 targets.

734 Given that both cell types project to both MeA and NAc, we sought to determine the
735 extent of collateralization in neurons composing the two pathways. To test whether plCoA-MeA
736 and plCoA-NAc projection neurons also project to multiple or overlapping downstream targets,
737 we employed a combination of retrograde Cre and Cre-dependent anterograde tracer viral
738 vectors. A retroAAV-hSyn-Cre-mCherry virus was into either MeA or NAc, and AAV-DIO-ChR2-
739 eYFP was injected into plCoA to label outputs of MeA- or NAc-projecting neurons (**Figure 6Q-R,**
740 **S8H-I**). We focused on MeA and NAc, as well as the ancillary primary downstream targets
741 implicated in valence or olfaction. We found different collateralization patterns for both
742 populations, where NAc-projecting neurons did not collateralize to MeA, but very strongly
743 collateralized to OT. In contrast, MeA-projecting neurons minimally collateralized to NAc and
744 most strongly collateralized to pmCoA (**Figure 6S-T**). Notably, neither projection of interest
745 significantly collateralized to the other. These data indicate that plCoA-MeA and plCoA-NAc
746 projection neurons are largely non-overlapping, spatially biased populations that output to
747 different downstream subnetworks.

748 **The plCoA neurons projecting to the NAc and MeA and Respectively Mediate Attraction**
749 **and Aversion to Odor**

750 The topographic separation of MeA- and NAc-projecting neurons are consistent with a
751 model of divergence valence that could support the observed topographic divergence
752 behaviors. To investigate the behavioral contributions of these projections, we first determined
753 whether the neurons projecting to the MeA and NAc are able to drive behavior with optogenetic
754 stimulation. We expressed ChR2 in a non-spatially biased manner by injecting AAV-hSyn-ChR2
755 into mplCoA, and we placed an optic fiber above MeA or NAc for selective optogenetic
756 stimulation at plCoA axon terminals (**Figure S3C**). We found that photostimulation of the plCoA-
757 MeA circuit in the four-quadrant open field task significantly reduced time spent in the 'on'
758 quadrant and increased the average distance to the corner port during the treatment period,
759 indicating activation of the plCoA-MeA circuit is aversive and leads to avoidance of the quadrant
760 paired with stimulation (**Figure 7A-D**). The opposite was true for the plCoA-NAc projection,
761 where stimulation in that zone instead increased the time in the 'on' quadrant and decreased
762 average distance to the corner port, indicating activation of the plCoA-NAc circuit is instead
763 appetitive and leads to attraction to the stimulation quadrant (**Figure 7B,E-F**). We next asked if
764 the effects of stimulating these circuits affected other non-valence behaviors by testing the mice
765 in the EPM and OFT. Using the EPM, we found no change in anxiety based on open arm time
766 or entries when stimulating either projection to the MeA or NAc (**Figure S11A-C,E-F,H-I**).
767 Similarly, stimulation in the OFT did not cause any change to thigmotaxis, based on time spent
768 in corners of the open field, or exploration, based on time spent in the center of the open field
769 (**Figure S11K-M,O-P,R-S**). Further, locomotion remained constant during stimulation across
770 both assays (**Figure S11D, S11G, S11J, S11N, S11Q, S11T**). These data indicate that the
771 divergent projections from plCoA to the MeA and the NAc are capable of driving valence-
772 specific behaviors without modulating anxiety.

773 Finally, we sought to determine whether plCoA-MeA or plCoA-NAc projecting neurons
774 are necessary for the expression of odor-evoked appetitive or aversive behaviors. To target
775 these projection neurons for chemogenetic silencing, we injected a retroAAV bearing an hSyn-
776 EBFP-Cre construct into MeA or NAc, along with an AAV in plCoA bearing a Cre-dependent
777 hM4D(Gi) construct (**Figure 7G,H**). This chemogenetic strategy was chosen over optogenetic
778 inhibition based on suitability for minutes-long inhibition and ease of movement in a closed
779 arena. We then tested the innate responses of these animals to 2PE or TMT in the four-
780 quadrant assay following administration of CNO or a vehicle control, as above. Inhibition of
781 plCoA-NAc projecting neurons abolished innate attraction to 2PE without having any effect on
782 aversion to TMT (**Figure 7I-L**). Conversely, inhibition of plCoA-MeA projecting neurons had no
783 effect on innate 2PE attraction, but significantly decreased the aversion to TMT (**Figure 7M-P**).
784 Silencing these neurons had no effect in the EPM and OFT assays, indicating the effects of
785 silencing these neurons are limited to valence or olfaction, and not anxiety or exploration
786 (**Figure S11M-X**). Thus, plCoA-MeA projecting neurons are necessary and sufficient for innate
787 aversion to TMT, whereas plCoA-NAc projecting neurons are necessary and sufficient for innate
788 attraction to 2PE.

789

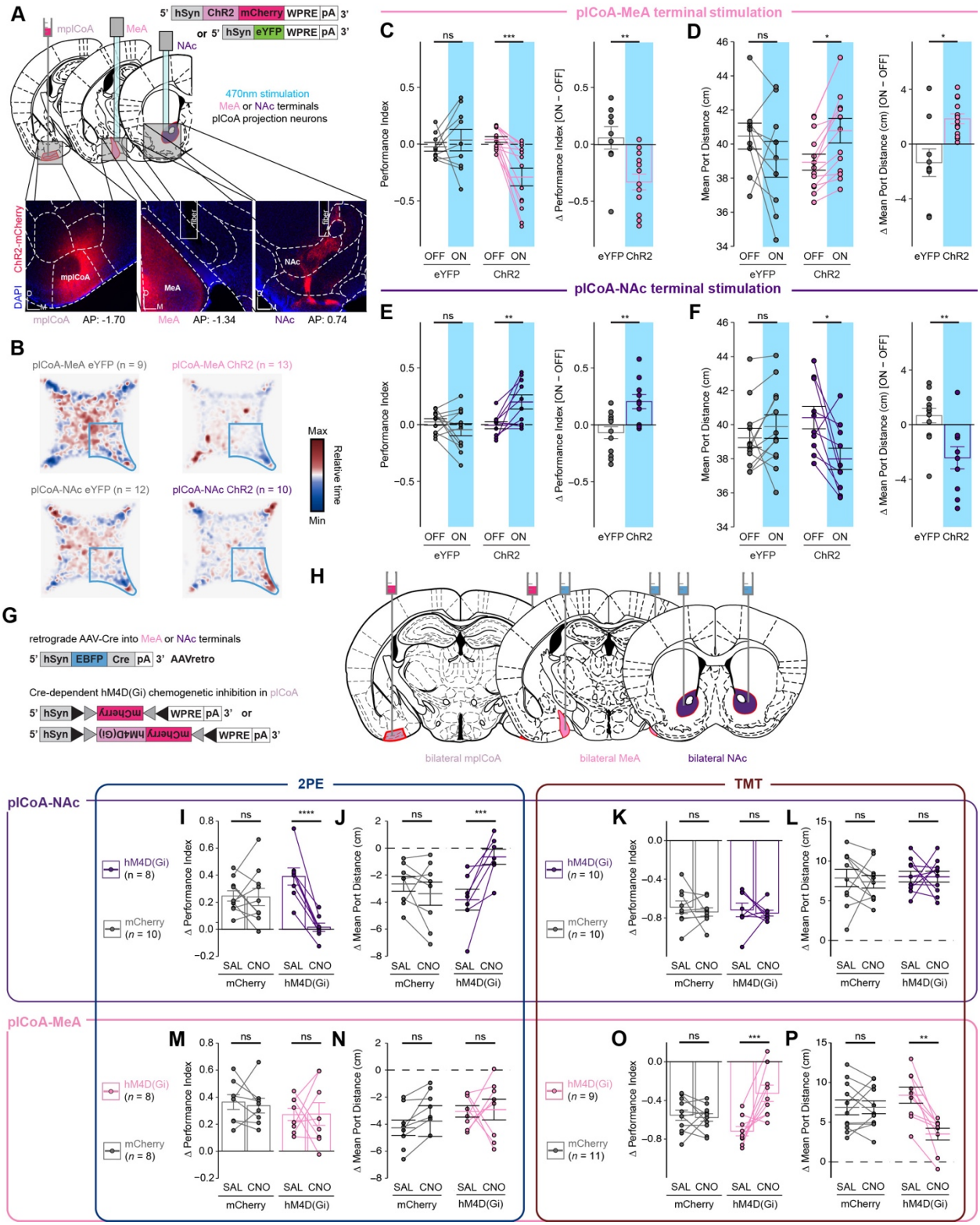
A
mplCoA
MeA
NAc
5' hSyn ChR2 mCherry WPRE pA 3'
or 5' hSyn eYFP WPRE pA 3'
470nm stimulation
MeA or NAc terminals
plCoA projection neurons
ChR2-mCherry
DAPI
mplCoA AP: -1.70
MeA AP: -1.34
NAc AP: 0.74
B
plCoA-MeA eYFP (n = 9)
plCoA-MeA ChR2 (n = 13)
plCoA-NAc eYFP (n = 12)
plCoA-NAc ChR2 (n = 10)
Max
Relative time
Min
plCoA-MeA terminal stimulation
C
D
Performance Index
Δ Performance Index [ON – OFF]
Mean Port Distance (cm)
Δ Mean Port Distance (cm) [ON – OFF]
OFF ON
eYFP
ChR2
plCoA-NAc terminal stimulation
E
F
G
retrograde AAV-Cre into MeA or NAc terminals
5' hSyn EBFP Cre pA 3' AAVretro
Cre-dependent hM4D(Gi) chemogenetic inhibition in plCoA
5' hSyn mCherry WPRE pA 3' or
5' hSyn mCherry hM4D(Gi) WPRE pA 3'
H
bilateral mplCoA
bilateral MeA
bilateral NAc
2PE
TMT
plCoA-NAc
plCoA-MeA
hM4D(Gi) (n = 8)
mCherry (n = 10)
hM4D(Gi) (n = 10)
mCherry (n = 10)
hM4D(Gi) (n = 8)
mCherry (n = 8)
hM4D(Gi) (n = 9)
mCherry (n = 11)
Δ Performance Index
Δ Mean Port Distance (cm)
SAL CNO
mCherry
hM4D(Gi)

790

Fig. 7. Divergent neurons projecting from plCoA to NAc and MeA control innate olfactory attraction and aversion.

(**A**) Schematic for optogenetic MeA terminal stimulation in plCoA neurons. Strategy to activate MeA-projecting plCoA neuron terminals via optogenetics (top) and representative histology from ChR2 viral injection and fiber implantation site (bottom).

(**B**) Baseline-normalized collective heatmaps from both the ChR2- and eYFP-infected plCoA groups with MeA- and NAc-localized fiber implants. Lower right stimulus quadrant marked in blue.

(C-D) Optogenetic MeA terminal stimulation of plCoA neurons infected with ChR2, but not eYFP, is sufficient to reduce time spent in the stimulation quadrant (**C**) and increase its average distance from the port (**D**) during the stimulation period.

(E-F) Optogenetic NAc terminal stimulation of plCoA neurons infected with ChR2, but not eYFP is sufficient to increase time spent in the stimulation quadrant (**E**) and decrease its average distance from the stimulation port (**F**) during the stimulation period.

(**G**) Viral strategy for selective retrograde chemoinhibition of projection-defined plCoA neurons.

(**H**) Schematic for selective retrograde chemoinhibition of projection-defined plCoA neurons.

(**I-L**) Chemoinhibition of NAc-projecting plCoA neurons significantly eliminates the 2PE-evoked increase in time spent in the odor quadrant (**I)** and decreases in mean port distance (**J).** The response to TMT is unaffected in time spent in odor quadrant (**K**) or port distance (**L**).

(**M-P**) Chemoinhibition of MeA-projecting plCoA neurons does not affect 2PE-evoked increase in time spent in the odor quadrant (**M)** or decrease in mean port distance (**N)** significantly decreases the TMT-evoked reduction in time spent in the odor quadrant (**O)** or increase in mean port distance (**P).**

Across panels, ns, not significant; * $p < 0.05$; ** $p < 0.01$; *** $p < 0.001$. Additional specific details of statistical tests can be found in Supplemental Table 1.

816 **DISCUSSION**
817 **Topographic Organization of Valence circuitry in plCoA**

818 The neural circuits mediating innate attraction and aversion to odor have not been fully
819 defined. Here, we have advanced our knowledge of the circuitry underlying innate olfactory
820 behaviors by defining its activity and organization within plCoA and further extending the innate
821 olfactory pathway from a third order olfactory brain area to limbic structures involved in
822 motivational valence. We have identified a novel functional axis for valence with the plCoA that
823 is defined by histologically and functionally distinct domains along the anteroposterior axis. We
824 have characterized odor encoding in plCoA, identifying a sparse population code for identity of
825 an odor, but not its innate valence, consistent with previous finding[15]. We have also
826 determined the composition of molecular cell types in plCoA and identified spatially biased
827 populations enriched within each domain, which we find sufficient to drive their respective
828 domain-specific behaviors, though only partially necessary for their functions in olfaction.
829 Moreover, we identified the outputs of plCoA and quantitatively characterized the relative
830 anatomical strength of each, as well as how it relates to plCoA topography and domain-specific
831 molecular cell types, demonstrating that neurons projecting to the MeA and NAc are
832 topographically and molecularly biased. Finally, we demonstrate that neurons projecting to the
833 to the NAc and MeA are capable of driving approach and avoidance responses, and loss of
834 function experiments demonstrate that the neurons projecting to the NAc or MeA selectively
835 support innate olfactory attraction and avoidance, respectively. Thus, plCoA is composed of
836 dissociable, spatially segregated ensembles for divergent valence, defined by their downstream
837 projection target. Though, it remains to be determined how broadly these neurons contribute to
838 the valence of other odors.

839 Spatial organization for features of sensory stimuli is common in sensory cortex, and has
840 been previously proposed as fundamental to sensory processing[36]. Visual cortex is
841 topographically organized by retinotopic locations in space, somatosensory cortex contains a
842 map of the body, auditory cortex has a crude tonotopic organization by frequency, and gustatory
843 cortex is segregated by taste qualities[23, 37-39]. However, topographic organization by
844 perceptual feature has not been observed in the olfactory system, which has been attributed to
845 the high dimensional nature of olfactory information[18]. Our findings identify a topographically
846 organized divergence motif for valence in plCoA, where activation of aplCoA evokes aversive
847 behavioral responses, and activation of pplCoA evokes attractive behavioral responses, with a
848 graded transition between the two domains (**Figure 2D-F**). This is consistent with prior studies
849 implicating a spatial organization to inputs from the OB to plCoA, where glomerulus-specific
850 anterograde tracing from OB shows specific glomeruli send fibers to invariant, densely
851 clustered, anatomically distinct locations within plCoA, and retrograde tracing from plCoA shows
852 that upstream glomeruli are spatially biased within OB[40] and closer examination reveals that
853 OB input can co-vary with plCoA anteroposterior position. Interestingly, spatial segregation of
854 divergent features is present elsewhere in olfaction as well, although not by perceptual feature.
855 Olfactory sensory receptors display stereotyped spatial organization within zones of the
856 olfactory epithelium, with a corresponding spatially-stereotyped glomerular topography in
857 OB[19, 41-43]. Further, these topographic domains in OB have functional relevance, where
858 region-specific OB manipulations selectively alter different olfactory behaviors[24, 44]. However,

859 the piriform cortex generally lacks apparent spatial organization or spatial patterning for odor
860 responses[18]. Thus, the topographical organization of valence observed here in plCoA
861 represents one of the first descriptions of these spatial patterns occurring in central olfactory
862 areas.

863 Topographic gradients for appetitive and aversive responses have been observed in
864 other limbic regions, including the BLA[22], the medial amygdala for innate social behaviors[45],
865 *Drosophila* dopaminergic mushroom body neurons for olfactory learning[46], and the gustatory
866 insular cortex for taste[47]. Our results extend this phenomenon of spatially segregated neurons
867 for valence into a less well-described amygdala nucleus, and suggest that it could serve as a
868 potential common motif within the limbic system to organize motivational information, especially
869 for innate behaviors, which require stereotyped neurocircuitry. We believe a model whereby
870 aplCoA and pplCoA are parts of the same region with similar underlying composition, but with a
871 gradual change in the factor that defines the valence output for a given part of the gradient
872 would best explain the underlying gradient-like effect on approach and avoidance. We
873 considered two such organizational principles underlying this topography: molecular cell types
874 and projection targets. We found that broad divisions of cell types by *VGluT*2 and *VGluT1* did
875 not fully define valence, though more specific subtypes could be responsible. Our results
876 indicate that the projection targets of plCoA neurons are a fundamental feature for imparting
877 valence on this circuitry.

878 **Molecular Cell Types in plCoA Segregate Topographically and Support Behaviors of**
879 **Divergent Valence**

880 While examining the cell types composing plCoA, we noticed numerous notable, novel
881 features. First, despite its small area (~1.04 mm^3 and ~170,000 cells [48]), plCoA displays
882 remarkable diversity, hosting dozens of distinct, robustly separable cell types[48]. The plCoA
883 appears to have multiple domains positioned at the transition between disparate brain tissue
884 types. Interestingly, the high-dimensional structure of molecular variation differs between
885 glutamatergic and GABAergic neurons. Glutamatergic molecular variation within plCoA is
886 continuous, with two broadly nested groups generally marked by either *VGluT2* or *VGluT1* along
887 with one or more additional marker gene(s), though it should be noted that expression of the two
888 broad glutamatergic markers is not necessarily mutually exclusive and a few low abundance
889 "transition" cell types can express both (**Figure 3E-F**). This leaves open the possibility that a
890 more specific cell type could be necessary for aversion, given that this necessity for this
891 behavior did not map onto either broad molecular cell type. In contrast, molecular variation in
892 GABAergic neurons is far more discretized, with ensembles expressing one of a few well-
893 characterized interneuron markers found throughout the brain, such as *Sst, Vip,* and *Pvalb*,
894 among others (**Figure 3G-H**). This is consistent with other studies in neocortex, hippocampus,
895 and subiculum that find similar patterns of variation, whereby variation within glutamatergic
896 neurons is more continuous than in GABAergic neurons[31, 49]. In this manner, we find the
897 continuous gradient-like structure of valence in plCoA is recapitulated with gradient-like variation
898 in glutamatergic neuron gene expression in plCoA.

899 In these molecular datasets, we further observed specific differences in cell type
900 enrichment within aplCoA and pplCoA within glutamatergic neurons, but not GABAergic
901 neurons or glia. Within plCoA, *VGluT2*+ neurons are enriched in aplCoA and *VGluT1*+ neurons
902 are enriched in pplCoA, though there is gradient-like intermingling of populations, especially
903 toward the middle of plCoA, and all glutamatergic neuron types are present, albeit with high
904 variability along the anteroposterior axis. This molecularly defined order suggests a
905 programmed organization, rather than stochastically distributed populations within the region,
906 especially given that its boundaries match the domains previously identified based on behavior
907 and histology[50]. This phenomenon also broadly matches observations in the neocortex,
908 hippocampus, and subiculum, where glutamatergic neurons across subdivisions molecularly
909 diverge to a greater degree than GABAergic neurons or glia, albeit across a correspondingly
910 greater area than within plCoA, which is generally accompanied by distinct morphological and
911 electrophysiological properties broadly corresponding to these transcriptomic differences[31, 32,
912 49, 51]. Spatial segregation of molecular cell types is also observed within deeper brain regions
913 including BLA, thalamus and habenula, and these molecular differences are also accompanied
914 by extended phenotypic differences[22, 52-54]. Investigation of such properties held in common
915 and diverging within and between *VGluT2*+ and *VGluT1*+ glutamatergic neuron types could also
916 serve to further define the local neurocircuitry and information processing dynamics within
917 plCoA and along its anteroposterior axis.

918 Interestingly, few if any populations within plCoA are clearly separable from most of the
919 regions surrounding it (e.g. piriform cortex, basomedial amygdala, and MeA) based on primary
920 marker gene identity. Instead, plCoA ensembles seem to be defined by the interplay of all three
921 regions within the same tissue. The predominance of populations resembling different regions
922 does appear related to this anteroposterior organization, though, where *VGluT2*+ neurons
923 predominate in both aplCoA and MeA, and more specific marker genes like *Meis2* are
924 expressed in both regions as well[55]. Conversely, *VGluT1*+ neurons predominate in both
925 pplCoA and piriform cortex, and the major marker genes like *Satb2* are similarly expressed in
926 both regions[56]. Such phenomena are also consistent with general characterizations made in
927 whole-brain molecular taxonomies, which divide plCoA along its axis, grouping aplCoA with
928 MeA and pplCoA with paleocortex[57-59]. It would be misleading to characterize plCoA
929 populations as mere extensions of surrounding populations into an adjacent region, though.
930 *VGluT1*+ neurons from the cortex-amygdala transition zone are also present in the dataset and
931 are continuously separable from *VGluT1*+ plCoA neurons based on the expression of marker
932 genes like *Fign*. Instead, plCoA may itself be a transition region, given that such a relationship
933 with its neighboring regions is very similar to that of the amygdalostriatal transition area, one of
934 the only transition regions to undergo high-resolution molecular profiling[60]. Given such
935 commonalities between these two putatively dissimilar regions, molecular characterization of
936 additional transition regions could potentially uncover similar organizational motifs, especially if
937 compared with adjacent regions of interest, and allow for a much more in-depth exploration and
938 characterization of the boundaries and transitions between proximally located, distantly related
939 brain regions.

940 These broad molecular groups of glutamatergic cell types themselves do not completely
941 explain valence in the plCoA. While aplCoA-enriched *VGluT2*+ neurons are sufficient to drive

942 aversion and pplCoA-enriched *VGluT1+* neurons are sufficient to drive attraction (**Figure 7A-F**),
943 as would be predicted from the valence responses evoked from each anterior-posterior domain
944 enrichments, it might be expected that these populations would also be necessary for the
945 respective odor-evoked valence. However, only *VGluT1+* neurons are necessary for 2PE
946 attraction, whereas the *VGluT2+* neurons were not required for aversion to TMT **Figure 7I-P**).
947 Given that the plCoA is necessary for TMT aversion, it is unlikely that such a difference is due to
948 additional redundant function within other regions for TMT aversion[14]. Rather, although
949 *VGluT2+* neurons likely contribute to aversion, other populations within the region not
950 expressing the marker gene could also contribute to the behavioral response. Thus, although
951 these two broad glutamatergic groups can drive innate responses of valence, the *VGluT2+*
952 population doesn't fully represent the population that control aversive responses, which is
953 supported by anatomic tracing presented here showing that both *VGluT2+* and *VGluT1+*
954 neurons project to MeA and NAc to different degrees (**Figure 6M-P, S9**). Regarding more
955 specific molecular cell types, it could be possible that only a subset of *VGluT1+* neurons are
956 required for 2PE attraction. Similarly, the neurons required for TMT aversion could be marked
957 by a gene orthogonal to the observed *VGluT*2/*VGluT*1gradient, and genetic access to olfactory
958 aversion could potentially be established by investigating these more sparsely expressed
959 marker genes. In both cases, though, further investigation into these other cell types would
960 enhance our understanding of both the plCoA and innate olfactory behavior and allow more
961 precise manipulations in the future.

962 **Divergent plCoA Neurons defined by Projection Targets Control Approach and**
963 **Avoidance**

964 In this work, we perform the first comprehensive characterization of plCoA's downstream
965 outputs in the mouse brain. These outputs are dominated by regions generally involved in
966 valence and emotion, such as the NAc, BNST, MeA, BLA, and other amygdalar nuclei, or
967 olfactory areas, such as the pmCoA, OT, and PIR (Figure 6A-D). These outputs are consistent
968 with a role for plCoA in motivational valence for odor. The plCoA also appears to form numerous
969 intra-regional connections, where a significant proportion of synapses formed with other
970 neurons are within the region itself. This raises the possibility that plCoA is not simply a
971 feedforward relay but performs local recurrent processing as well. Recurrent networks in other
972 sensory systems expand the dimensionality of encoding schemata and incorporate additional
973 features to generate mixed, continuously updating representations of relevant information[61].
974 This raises a number of interesting questions regarding information processing within plCoA.
975 For instance, how does odor representation change based on differences in experience and
976 internal state? Further explorations of information transformation and encoding within plCoA will
977 enrich our understanding this region.

978 The NAc and MeA are interesting downstream targets given their known relationships to
979 appetitive and aversive responses, respectively. NAc has historically been critical to the
980 manifestation and processing of reward and motivated behaviors, though this view has been
981 expanded and made more nuanced with a recent focus on action selection[62]. On the other
982 hand, MeA has been linked to defensive and stress-related behaviors in response to aversive
983 stimuli. MeA has also been specifically linked to olfactory aversion in past studies, as TMT has

984 previously been shown to activate the MeA[63], which is necessary for TMT-induced defensive
985 behaviors[34], though the upstream circuits and processing were not yet investigated. These
986 circuits are also notable regarding other features of plCoA spatiomolecular organization, as the
987 projections to the downstream regions of interest are the two that diverge to the greatest extent
988 between aplCoA and pplCoA, and between plCoA$^{VGluT2+}$ and plCoA$^{VGluT1+}$ glutamatergic
989 neurons. Given the relationship between spatiomolecular patterning and the simple wiring and
990 organizational rules used to structure innate circuits it would be interesting to investigate the
991 plCoA through the lenses of development and genetic variation. These intersect in recent
992 discussions of genetic bottlenecking, where the genome encodes general rules for circuit
993 organization and development that nevertheless yield specific responses to specific stimuli[64].
994 Such networks have numerous theoretical advantages, such as reduced information
995 requirements and higher performance at criterion, providing a conceptual basis for why
996 spatiomolecularly stereotyped circuits yield innate behaviors, and why these innate behaviors
997 are adaptive in naturalistic settings[64-66].

998 **Neuronal Activity in plCoA Encodes Odor Identity Via Sparse Population Code**

999 The plCoA receives spatially-ordered inputs and has a cell-type-specific topographical
1000 organization with divergent outputs that mediate approach and avoidance responses. This
1001 anatomical organization is consistent with either labeled-line or divergent paths motifs, though
1002 precise connectivity from OB has not yet been described. However, labeled line coding motif is
1003 not apparent in neural activity, but instead there is a sparse population code for odor identity
1004 with no apparent valence-specific responses, indicating that the plCoA cannot function as a
1005 pure labeled-line relay. Moreover, the absence of valence encoding is distinct from that seen in
1006 other divergent path motifs, suggesting the plCoA represents a different circuit model for
1007 valence.

1008 We were surprised to find that despite a robust organization of plCoA cell types and
1009 projections that support approach and avoidance behaviors, the neurons do not appear to
1010 encode appetitive and aversive responses at the single neuron or population level (**Figure 1**).
1011 However, when put in the context of the olfactory system, these results are less surprising.
1012 Sparse, distributed population encoding appears to be a general feature of all olfactory regions
1013 observed thus far, regardless of their specific structure or computational function within
1014 olfaction. In the OE, OSNs expressing a single receptor will bind multiple odorants and establish
1015 odor identity through a combinatorial code.[21,23] In the OB, axon terminals from OSNs expressing
1016 the same receptor converge into specific stereotyped glomeruli, where mitral/tufted cells (M/T)
1017 then transmit this information to third-order olfactory regions. Both layers represent the odor
1018 identity via a sparse population code in a spatially-distributed manner[19, 67]. The primary
1019 olfactory cortex further represents odor identity through sparse, spatially distributed
1020 combinatorial population activity in a similar manner[18]. The OT, a striatal region primarily
1021 composed of *Drd1*- or *Drd2*-expressing medium spiny neurons, also broadly represents odor
1022 identity across both cell types, despite their opposing roles elsewhere in striatum, and a
1023 contribution to learned hedonic value is currently debated[20, 68]. Although direct comparisons
1024 of olfactory regions find some differences in features like sparsity, clustering, or correlation
1025 structure, these are generally reported as differences in degree, not in kind. Given the

remarkable similarity in encoding between these structurally and functionally distinct regions, it logically follows that an olfactory region with amygdalar structure would follow similar population encoding principles. Indeed, were plCoA to predominantly encode stimulus valence in a manner akin to other amygdalar regions, it would reflect a greater divergence from olfactory coding principles than what we observe. Instead, the olfactory encoding scheme employed by plCoA reveals a framework for valence encoding that is distinct from that in the extended amygdala.

How does innate valence arise from a population code imposed on stereotyped circuitry? One possibility is that the valence of an odor is defined by the proportion of NAc and MeA-projecting neurons activated, mixing features of divergent paths and opposing components motifs. In this model a given odor should activate some balance of NAc and MeA projecting neurons and the proportional balance determines the behavioral response (**Figure 8A**). The activation of TMT labeled neurons (**Figure S4**) in different domains is consistent with this model. That is if the valence is determined by the balance of activation of NAc and MeA projecting neurons, then activating a subset of that balance in the anterior and posterior should drive the valence specific response, which is indeed what we observe. If true, one should also be able to predict the valence of the odor by recording from a large sample of these projection-defined neurons. A similar model has also been proposed in the OB[69]. Another possibility is that activity could evolve over the time course of behavior in freely moving animals such that a mixture of inputs from local circuitry and long-range circuits could function like attractor networks to shape output into one of a few convergent states (**Figure 8B**), consistent with attractor networks in the hypothalamus[70]. A third possibility is that valence may emerge in combination with behavior and internal state. In this model, the plCoA integrates sensory information with other state variables to shift the activity towards one output. If either of these latter two models is correct, recording activity over longer time scales in freely moving animals could provide insight into how activity correlates with behavior. Alternatively, valence signals may arise downstream of plCoA, but molecular mechanisms to support this model are currently undescribed, and such a model would be at odds with our finding of divergent valence-specific circuitry required attraction and aversion. Moreover, innate behavior is dynamic and more complex than simple attraction and avoidance and it is possible that the neural activity is as dynamic, changing over the course of behavior. Thus, it will be important to investigate activity of in the plCoA in behaving animals.

A unique amygdala circuit motif for valence using a population code

The widespread circuit model for valence encoding centers on divergence, in which information is routed to different pathways depending on the valence of the stimulus. The plCoA circuit we have identified is anatomically similar, but unique in its encoding properties. Most divergent circuits function to generalize stimuli, discarding information about stimulus identity to simplify to low dimensional valence signals from distinct neuronal populations. In contrast, the plCoA groups stimuli, using a high dimensional code of odor identity that appears to be routed through divergent projections to mediate opposing responses. In this model, the valence of an odor could be determined based on the population dynamics and composition within a distributed, sparse population code that ultimately funnels information through divergent

pathways corresponding to their innate significance. Such a model could serve to increase the flexibility of the system while retaining the ability to yield stereotyped responses.

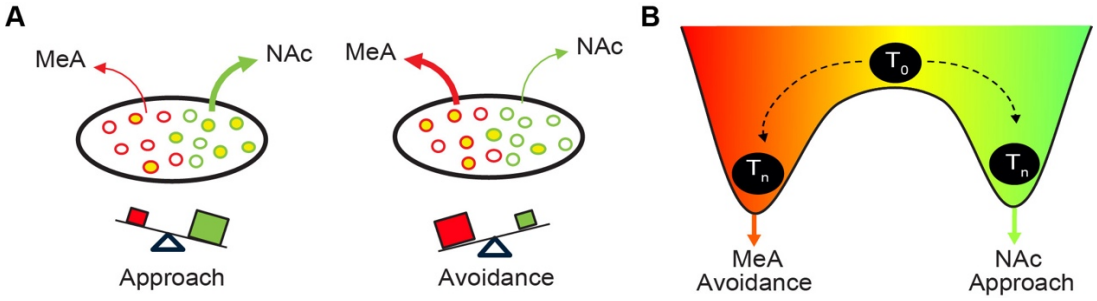

Figure 8. Models that could support innate odor evoked attraction and avoidance. Two potential models that could support valence responses to odor with a population code imposed on divergent circuitry.
(**A**) Balance of activation between MeA- and NAc-projecting neurons determines the valence. In this model an odor may activate a different proportion of these projection-defined neurons, and the valence is determined by the balance. For example, activation of more NAc-projecting neurons should cause attraction, and activation of more MeA-projecting neurons should cause aversion.
(**B**) Dynamic activity evolves overtime due to recurrent processing or integration of behavioral state variables, in an attractor-like network. In this model, the activity may evolve from an initial broad population code (T_0) towards preferential activation of one output population over time (T_n).

1082 **Limitations of the study**

1083 The odorant, TMT, is a thiol containing odorant and has long been suspected of acting
1084 as an irritant through the trigeminal system and it is known to activate TrpA1 channels in
1085 trigeminal neurons[71]. However, other work has shown that removal of the olfactory bulb or
1086 $ZnSO_4$ disruption of OSNs eliminates TMT evoked freezing, whereas lesion of the trigeminal
1087 nerve does not[72, 73]. Further, in our assay, TMT avoidance requires the olfactory bulb, and
1088 plCoA circuitry indicating the involvement of the olfactory system in TMT evoked behaviors[14].
1089 Thus, despite the differences in observations in underlying pathways for TMT responses, the
1090 aversion measured in our assay is dependent on olfactory pathways but there is a potential for it
1091 to also engage the trigeminal pathway.

1092 The conclusion that the plCoA circuitry mediates approach and avoidance is limited by
1093 the use of only one attractive and one aversive odor in our behavioral experiments. Thus, it
1094 remains unclear how these findings generalize to other odors. The fact that exogenous
1095 activation of different pathways is sufficient to produce behaviors of opposite valence suggests
1096 that there are dedicated plCoA outputs for different behaviors, but the broader necessity
1097 remains to be tested. Moreover, it remains unclear how odor activates neurons with distinct
1098 projections. Although we did not observe generalized valence responses to odor in calcium
1099 imaging experiments, our investigation only concerns the activity of general plCoA ensembles,
1100 not of specific neurons. Thus, it remains possible that neurons projecting to the NAc or MeA are
1101 more likely to respond to attractive or aversive odors, respectively. However, we did not observe
1102 any bias in odor response based on topographical location, and projection defined neurons are
1103 topographically distributed.

1104 The lack of valence encoding may also be an artifact of head-fixation, in which mice do
1105 not reliably exert the full repertoire of innate behaviors and are unable to use behavior to
1106 approach or avoid the odor. Both internal state and environmental context are known to
1107 influence sensory processing[74-76], raising the possibility that odor responses are altered
1108 under head-fixed conditions, thereby modifying the apparent tuning properties of plCoA
1109 neurons. Odor valence itself may also lose behavioral relevance when the animal cannot
1110 approach or avoid the stimulus. Future work will benefit from recording neural activity in freely
1111 moving animals to determine whether valence-related tuning emerges under more naturalistic
1112 conditions.

1113 We provide evidence that plCoA projections to the NAc and MeA are necessary and
1114 sufficient for attraction and avoidance. However, an intersectional chemogenetic approach
1115 silences the neurons projecting to a given target, not just the specific projection. It is possible
1116 that collaterals from MeA-projecting plCoA neurons contribute to the behavior. However, given
1117 that NAc and MeA projection neurons do not co-collateralize, it is reasonable to consider the
1118 pathways as distinct from each other. Lastly, it remains unclear what the projections from the
1119 plCoA to other areas contribute to odor evoked behavior. For instance, the BNST and LS have
1120 been implicated in a variety of functions including stress, arousal, anxiety, and social behaviors.
1121 Thus, it is possible that those projections mediate aspects of behavior beyond attraction and
1122 avoidance that were not assessed in our assay.

1123

ACKNOWLEDGMENTS

We thank the entire Root lab for helpful discussion and support. We thank B. Lim for provision of the AAVDJ-hSyn-Flex-mRuby-T2A-SynEGFP virus. We thank G. Pekkurnaz, N. Spitzer, and M. Pratelli for reagents and facilities support. We also thank C. O'Connor and L. Boggeman at the Salk flow cytometry core, and N. Hah at the Salk next-generation sequencing core. We thank D. Jimenez for assistance with histology and colony management. This publication includes data generated at the UC San Diego IGM Genomics Center utilizing an Illumina NovaSeq 6000 that was purchased with funding from a National Institutes of Health SIG grant (#S10 OD026929). This work was generously supported by the National Defense Science and Engineering Fellowship (J.R.H.), CIHR Postdoctoral Fellowship (F.M.), JPB Foundation, the PIIF, PNDRF, JFDP, New York Stem Cell Foundation, Klingenstein Foundation, McKnight Foundation, Salk Institute, Howard Hughes Medical Institute, Clayton Foundation, Kavli Foundation, Dolby Family Fund (K.M.T.), the Hellman Fellowship (C.M.R.), and the National Institutions of Health, via grants through the NIA (RF1AG061831-01S1, P.A.D.), NIMH (K99MH121563-02, F.M.; R01MH115920-03 and R37MH102441, K.M.T.), NIDDK (DP2DK102256-01S1, K.M.T.), and NCCIH (DP1AT009925-04, K.M.T.), and the NIDCD (R00DC014516-05 and R01DC018313-01A1, C.M.R.).

AUTHOR CONTRIBUTIONS

J.R.H., C.L.C and C.M.R. conceived the project. J.R.H., C.L.C., D.L., M.B., J.H.L. L.D., and A.N.Z. performed surgeries and analyzed histological data. J.R.H., C.L.C., and A.N.Z. performed behavioral experiments, managed the colony, and analyzed behavioral data. J.R.H. and D.L. performed calcium imaging experiments and analyzed calcium imaging data. J.R.H. performed sequencing experiments, analyzed sequencing data, and prepared all figures. H.K.R. and P.A.D. designed and performed spatial transcriptomics experiments and provided data for analysis. F.M., M.E.L., and K.M.T. provided the CellProfiler processing pipeline, as well as intellectual, facilities, and logistic support and guidance. C.M.R. supervised the project. J.R.H., D.L., M.B., H.K.R., and C.M.R. wrote the manuscript. All authors edited the manuscript.

DECLARATION OF INTERESTS

The authors declare no competing interests.

RESOURCE AVAILABILITY

Lead contact

Further information and requests for resources and reagents should be directed to and will be fulfilled by the Lead Contact, Cory M. Root (cmroot@ucsd.edu).

Materials availability

This study did not generate new unique reagents.

Data and code availability

All snRNA-seq and Visium spatial sequencing data generated for this study is deposited on Gene Expression Omnibus (GEO): GSE270798. All other data reported in this paper will be shared by the lead contact upon request. The code used to analyze all data and generate all graphs can be found online at Zenodo: Any additional information required to reanalyze the data reported in this paper is available from the lead contact upon request.

EXPERIMENTAL MODEL AND SUBJECT DETAILS

All procedures at the University of California, San Diego, and Columbia University were performed in accordance with Institutional Animal Care and Use Committee protocols in accordance with NIH guidelines. All mice were provided food and water ad libitum and maintained on a regular 12-hour reverse light/dark cycle at room temperature, with weight, health, and immune status monitored daily and verified to be within normal ranges. Mouse cages were changed regularly based on degree of soiling. All mice were group-housed with randomly assigned littermates prior to surgery, and single-housed after surgery. All animals were used in a single experiment each, except for a subset of mice who underwent 4-quad, EPM, and OFT experiments, who performed each test in no specific order.

Subject Details for Sequencing Experiments

Subject details for single-nucleus sequencing

All mice for snRNA-seq in the study were males on the wild-type C57BL/6J background (RRID:IMSR_JAX:000664) and received directly from Jackson Laboratories at 6 weeks of age and acclimated to the colony prior to experiments. Animals were single-housed and placed into sensory deprivation 24 hours prior to sacrifice to reduce artifactual immediate early gene expression. Sacrifice was performed at P60 ± 3 days (n = 5-10 mice per pool). Sample size was determined based on number of expected nuclei per region per mouse: estimates of expected nuclei were determined empirically, though nuclear recovery was approximately 20% of total based on cellular density estimates from the Blue Brain Cell Atlas. 20,000 nuclei were targeted per combination of assay, condition, and region, which was determined using SCOPIT v1.1.4, allowing potential detection of at least 10 nuclei from 10 rare subpopulations at 0.1% frequency with 95% probability[77]. A total of 50 mice were used for this purpose.

Subject details for spatial transcriptomics

In the separate study for spatial transcriptomics, APP23 (B6.Cg-Tg(Thy1-APP)3Somm/J; C57BL/6J background, RRID:IMSR_JAX:030504) non-transgenic (NTG) littermates control mice were housed in light-tight enclosures[78]. The mice were given ad libitum food and water access. This study used a total of 17 mice almost equally distributed across sex, of which sections from 11 sagitally bisected the plCoA and were used in downstream analysis. No analysis of sex differences was performed due to inaccessibility of that information on a per-

section basis. However, no such differences were apparent from per-section gene expression correlations reported in supplementary information.

Subject Details for Calcium Imaging, Tracing, and Activity Manipulations

Subject details for wild-type experiments

All mice for topographic and projection-defined manipulation and tracing experiments, as well as calcium imaging, were males on the wild-type C57BL/6J background and received directly from Jackson laboratories before 12 weeks of age. After surgery, mice incubated for at least 21 days if injected with virus or at least 7 days if injected with a retrograde tracer (e.g. retrobeads, cholera toxin B) to allow virus to express and tracers to travel in retrograde, respectively. All surgeries and downstream experiments were performed on mice at least 8 weeks of age.

Subject details for transgenic experiments

We used VGlut2-IRES-Cre (Slc17a6tm2(cre)Lowl; C57BL/6J background, RRID:IMSR_JAX:028863; *Slc17a6::Cre*) and VGlut1-IRES2-Cre-D (Slc17a7tm1.1(cre)Hze; C57BL/6J background, RRID:IMSR_JAX:023527; *Slc17a7::Cre*), Arc-CreER^{t2} (RRID:IMSR_JAX:022357) strain mice for molecularly defined optogenetic stimulation experiments and genotype-specific tracing. These mice were bred on-site at UCSD and were genotyped in-house using genomic DNA from ear tissue amplified with the default primer sets listed by Jackson Laboratories. All mice used for experiments had a heterozygous genotype for the transgenic construct of interest. After surgery, mice incubated for at least 21 days to allow viral expression.

METHODS DETAILS

Stereotactic surgery procedures

All surgeries were performed under aseptic conditions using a model 1900 digital small animal stereotaxic instrument (Kopf Instruments). Mice were initially anesthetized in a sealed box containing 5% gaseous isoflurane, and then deeply anesthetized using isoflurane (2.5% in 1L/min of O_2) during surgeries (VetFlo, Kent Scientific Corporation). We immobilized and leveled the head in a stereotaxic apparatus (Kopf Instruments), removed fur from the scalp by shaving, applied eye lubricant (Optixcare), cleaned the incision site with 70% ethanol and betadine prior to incision, peeled off connective tissue, and dried the surface of the skull prior to craniotomy before proceeding with injections and implantations specific to certain experiments. All virus injections were performed at 2 nL/sec using a pulled glass pipette (Drummond) and a Nanoject III pressure injector (Drummond). To prevent backflow, the pipette was left in the brain for 15 minutes after injection.

Surgeries for calcium imaging

1229 Surgeries for imaging experiments were performed in a manner similar to that previously
1230 described[20]. The skull was prepared with OptiBond™ XTR primer and adhesive (KaVo Kerr)
1231 prior to the craniotomy. After performing a craniotomy 1 mm in diameter centered around the
1232 virus injection site, a 27G blunt needle was used to aspirate ~2.5 mm below the brain surface.
1233 600 nl of AAV9-hSyn-FLEX-jGCaMP8s-WPRE (2.5×10^{13} gc/ml, Addgene) was diluted to ~$1 \times$
1234 10^{12} gc/ml gc/ml and injected into the left middle plCoA in two 300 ul boli, one in layer 2 and one
1235 400 um dorsal (+0.4 DV) in layer 3. Following the viral injection, a head-plate (Model 4,
1236 Neurotar) was secured to the mouse's skull using light-curing glue (Tetric Evoflow, Ivoclar
1237 Group). At least 30 minutes after viral injection, a 1 mm GRIN lens (NA, ~1.9 pitch, GrinTech)
1238 was sterilized with Peridox-RTU then slowly lowered at a rate of 500 um/min into the craniotomy
1239 until it was 200 um dorsal (+0.2 DV) to the injection coordinate. The lens was adhered to the
1240 surface of the skull using Tetric Evoflow. We then placed a hollow threaded post (AE825ES,
1241 Thorlabs) to act as a housing for the lens and adhered it using Tetric Evoflow. Any part of the
1242 skull that was still visible was covered using dental cement (Lang Dental). Finally, the housing
1243 was covered with a Nylon cap nut (94922A325, McMaster-Carr) screwed onto the thread post to
1244 protect the lens in between imaging. Animals were left on the heating pad until they fully
1245 recovered from anesthesia.

1246 ***Surgeries for optogenetic stimulation***

1247 For optogenetic topographic- or projection-specific stimulation experiments, we injected wild-
1248 type C57BL/6J mice between 2-4 months of age with 100 (if topographic) or 150 (if projection-
1249 specific) nL of either AAV5-hSyn-eYFP (3.3×10^{12} gc/ml, UNC Vector Core) or AAV5-hSyn-
1250 ChR2-mCherry-WPRE-PA (4.1×10^{12} gc/ml, UNC Vector Core). For Cre-dependent molecularly
1251 defined optogenetic stimulation, we injected 200 nl AAV5-EF1A-DIO-hChR2(H134R)-eYFP (5.5
1252 $\times 10^{12}$ gc/ml, UNC Vector Core) or AAV5-EF1A-DIO-eYFP (4.0×10^{12} gc/ml, UNC Vector Core)
1253 All such injections were left unilateral, into either aplCoA or pplCoA for topographic
1254 photostimulation, and into middle plCoA for projection- or genotype-specific photostimulation.
1255 For topographic and genotype-specific photostimulation animals, we implanted the fiber 300 um
1256 (+0.3 DV) directly above the injection site with all other coordinates remaining constant.
1257 Anterior-posterior axis positioning arose from stochastic variation in virus and fiber placement.
1258 For projection-specific photostimulation animals, we implanted the fiber 300 um (+0.3 DV)
1259 directly above either the MeA or NAc, holding all other coordinates for the two regions constant
1260 as described above. For all optogenetic stimulation experiments, we implanted a fiber optic
1261 cannula (2.5 mm ferrule outer diameter, 200 um core, 0.39 numerical aperture; RWD) 300 um
1262 above the targeted stimulation site. These fibers were affixed onto the skull using OptiBond XTR
1263 (Kerr) and stably secured with Tetric Evoflow (Ivoclar Vivadent) coated with cyanoacrylate
1264 (Toagosei). After surgery, we injected all mice with 0.04 mL Buprenorphine SR (Ethiqa XR,
1265 Fidelis) for pain management. All mice were singly housed immediately after surgery and
1266 returned to the colony once ambulatory.

1267 ***Surgeries for chemogenetic inhibition***

1268 For all plCoA inhibition experiments, we bilaterally injected C57BL/6J mice between 2-4 months
1269 of age with 250 nL of either AAV2-hSyn-DIO-hM4D(Gi)-mCherry (7.1×10^{12} gc/ml, Addgene) or

1270 AAV2-hSyn-mCherry (1.8 × 10^{13} gc/ml, Addgene) virus. For projection-specific inhibition
1271 experiments, wild-type C57BL6/J mice were used, and AAVretro-hSyn-EBFP-Cre (1.5 × 10^{12}
1272 gc/ml, Addgene) either 50 nL were injected into MeA or 300 µL were injected into NAc. For
1273 genotype specific inhibition experiments, *VGluT2::Cre* or *VGluT1::Cre* mice were used. All
1274 injections were bilateral and targeted to middle plCoA.

1275 ***Surgeries for fluorescent tracing***

1276 For non-topographic anterograde tracing experiments, we bilaterally co-injected of mixed 50 nl
1277 AAVDJ-hSyn-FLEX-mRuby-T2A-SynEGFP (4.0 × 10^{12} gc/ml, Addgene, a gift from Byungkook
1278 Lim) and AAV5-EF1A-mCherry-IRES-Cre-WPRE (1.9 × 10^{12} gc/ml, UNC Vector Core) into
1279 middle plCoA (-1.8 AP, +/-2.9 ML, -5.95 DV).[105,106] For topographic anterograde tracing
1280 experiments, we unilaterally injected 20 nl AAV8-hSyn-hChR2(H134R)-mCherry (2.1 × 10^{13}
1281 gc/ml, Salk GT3 Viral Vector Core) and AAV8-hSyn-hChR2(H134R)-eYFP (3.2 × 10^{13} gc/ml,
1282 Salk GT3 Viral Vector Core) into aplCoA (-1.4 AP, -2.8 ML, -5.95 DV) and pplCoA (-2.1 AP, -3.0
1283 ML, -5.95 DV), counterbalancing region by fluorophore. For retrograde topographic tracing
1284 experiments, we unilaterally injected Red Retrobeads IX (Lumafluor) into either MeA (50 nl, -1.2
1285 AP, -2.0 ML, -5.5 DV) or NAc (+1.1 AP, -1.35 ML, -4.5 DV), at volumes of 50 nl or 300 nl,
1286 respectively. For anterograde collateralization experiments, AAVretro-EF1A-IRES-Cre (1.3 ×
1287 10^{13} gc/ml, Addgene) into either MeA or NAc, and AAVDJ-EF1A-DIO-hChR2(H134R)-eYFP-
1288 WPRE-pA (4.03 × 10^{13} gc/ml, Salk GT3 Viral Vector Core) was injected into middle plCoA. For
1289 genotype-specific anterograde tracing experiments we injected 50 nl AAVDJ-Ef1a-DIO-
1290 ChR2(H134R)-eYFP-WPRE-pA into middle plCoA in VGluT2::Cre or VGluT1::Cre mice.

1291 ***Arc-cre labeling of neurons***

1292 For experiments using Arc-CreER^{T2} mice, odor responsive neurons were labeled as previously
1293 described[14]. One week after the viral injection and fiber implantation the mice were placed in
1294 clean cage housed in an isolated quite and dark enclosure for 1 day prior to odor exposure.
1295 Mice were administered tamoxifen (2 mg/ml in a solution of 10% ethanol and 90% corn oil) by
1296 intraperitoneal injection. Six hours after tamoxifen injection they were exposed to TMT (1 µL) on
1297 a cotton swab placed in their cage for 5 minutes.

1298 **Calcium Imaging**

1299 ***Odor exposure***

1300 Odor exposure for imaging experiments was adapted from methods previously described[20].
1301 Odor was delivered to the mouse using a custom-built olfactometer. Compressed medical air
1302 was split into 2 gas-mass flow controllers (Aalborg). One flow controller directed a constant rate
1303 of 1.5 L/min to a hollowed out teflon cylinder. The other flow regulator was connected to a 3-way
1304 solenoid valve (The Lee Co.). Prior to odor delivery, the 3-way valve directed clean air at 0.5
1305 L/min to the teflon cylinder. During odor delivery, the 3-way valve directs air to an odor manifold,
1306 which consists of an array of 2-way solenoid valves (The Lee Co.), each connected to a
1307 different odor bottle. The kinetics and consistency of odor delivery were characterized using a
1308 miniature Photoionization Detector (mPID) (Aurora Scientific) mounted above the odor port. The

1309 odors were detected using different gain settings on the PID control box as follows: 1x for TMT
1310 and 4MT, 5x for IAA, 10x for Peanut, 2PE and Heptanol. Depending on the trial type, the
1311 appropriate 2-way valve opens, directing 0.5 L/min of air flow through the odor bottle containing
1312 a kimwipe blotted with 20 ul of odorant, except for 2PE and peanut oil, in which 500 ul was
1313 used.

1314 Prior to imaging, mice were habituated to the head fixation device (Neurotar) and treadmill for at
1315 least 3 days for at least 5 minutes per session beginning at least 10 weeks after surgery. The
1316 treadmill parts were 3D printed using an LCD printer (EPAX) from publicly available designs.
1317 Walking behaviors were measured using a quadrature encoder (Broadcom). A video feed of the
1318 animal's face was also recorded using a camera (Basler) with an 8-50mm zoom lens (Arducam)
1319 at 20 Hz with infrared illumination (Lorex Technology). Animals were exposed to the following
1320 odors for 5 seconds: the appetitive odors 2-phenylethanol (Sigma-Aldrich) and peanut oil
1321 (Spectrum), the neutral odors 1-heptanol (Sigma-Aldrich) and isoamyl acetate (Sigma-Aldrich),
1322 and the aversive odors trimethylthiazoline (BioSRQ) and 4-methylthiazole (Sigma-Aldrich).
1323 Within a single contiguous exposure session, each of the 6 odors were provided 20 times with
1324 12-18 seconds of inter-trial interval. Trials were organized into 6 blocks, each of which consisted
1325 of 20 trials of each of the 6 odors in counterbalanced order without any odors of similar innate
1326 valence adjacent to each other in the trial structure.

1327 ***2-photon microscope data acquisition***

1328 Ca^{2+} imaging data was acquired using an Olympus FV-MPE-RS Multiphoton microscope with
1329 Spectra Physics MaiTai HPDS laser, tuned to 920 nm with 100 fs pulse width at 80 MHz. Each
1330 128 × 128 pixel scan was acquired with a 20x air objective (LCPLN20XIR, Olympus), using a
1331 Galvo-Galvo scanner at 5 Hz. Stimulus delivery and behavioral measurements were controlled
1332 through a custom software written in LabVIEW (National Instruments) and operated through a
1333 DAQ (National Instruments). Each imaging session lasted up to 90 minutes and was
1334 synchronized with the stimulus delivery software through a TTL pulse. Animals were excluded
1335 from analysis if histology showed that either the GRIN lens or the jGCaMP8s virus was
1336 mistargeted or the motion during imaging was too severe for successful motion correction.

1337 **Behavioral Assays**

1338 Mice had been handled for 5 days prior to experiments and acclimated to the room for an hour
1339 prior to testing. All behavioral experiments were performed during the dark period of the
1340 light/dark cycle at least an hour away from the switch between the two photoperiods. Not all
1341 mice were run in all assays, as elevated plus maze and open field tests were added after a
1342 significant proportion of four-quadrant data was collected at targeted sample sizes and mice had
1343 already been sacrificed.

1344 For all optogenetic experiments, optical fibers (200 mm, 0.39 numerical aperture, Thorlabs)
1345 were epoxied to 2.5 mm stainless steel ferrules (Precision Fibre Products), and polished with a
1346 fiber optic polishing kit (Thorlabs) to achieve a minimum of 80% transmission. After surgical
1347 implantation, the ferrules protruding from the mouse's head were coupled to an ADR-800A 100

mW 473 nm laser (LaserCentury) via custom-made patch cables with a single rotary joint (Doric Lenses) between the mouse and laser. Laser intensity was set to 5-8 mW at the end of the patch cable. For inhibition experiments, all mice were injected intraperitoneally 60 minutes prior to the beginning of the behavioral trial with either sterile PBS vehicle or with clozapine-N-oxide (CNO) dihydrochloride (Hello Bio) dissolved in sterile PBS for a dosage of 2 mg/kg.

Four quadrant open field assay

The four-quadrant open-field task was performed as previously described[14]. In short, all behavioral assays took place in a four-quadrant open field chamber. Airflow was pumped into each quadrant via gas-mass flow controllers 150 mL/min (Cole-Parmer). Airflow exited the chamber via a 1-inch outlet in the center of the chamber's floor covered by steel mesh, and the outlet was connected a vacuum line with a gas-mass controller set to 750 mL/min. The chamber was housed in the dark and illuminated from below by infrared lighting. A Basler A601FM camera (Edmund Optics) mounted above the chamber recorded videos of behavioral trials at 4 Hz, and custom software written in Labview (National Instruments) tracked the position of the mouse in real time for each frame. The symmetrical four-quadrant open field chamber was contained in a lightproof structure (0-10 lux) and illuminated by infrared lights, removing any potential spatial cues available to the animals with respect to the room or its surroundings. In optogenetic experiments, an additional 5 cm spacer was added to the chamber flush with the walls to raise their height for more naturalistic behavior, and an acrylic ceiling with a top with a circular opening 30.5 cm in diameter was added to prevent escape while allowing the fiber optic cable to move freely.

In optogenetic experiments, the laser was pulsed with 50 ms bins at 10 Hz, and there was a steep gradient from 1 to 10 Hz along the perimeter of the quadrant, increasing as proximity to the corner of the quadrant decreased. Preliminary experiments in topographical stimulation animals identified no clear behavioral effects from the location of the stimulus quadrant itself (data not shown), and all other downstream stimulation experiments exclusively used the lower right quadrant for stimulation to simplify data analysis. The lasers were controlled by TTL modulation from custom Labview software synchronized to the video capture system.

For inhibition experiments, odor was applied by solenoid valves redirecting airflow through 100 mL glass bottles containing 1 μL of a pure odorant on a small piece of Kimwipes. Odorants used were either the previously-validated innately aversive 2,5-dihydro-2,4,5-trimethylthiazoline (BioSRQ) or the innately appetitive 2-phenylethanol (Sigma-Aldrich) on a small piece of Kimwipe.[10] All odors were presented in the lower-right quadrant, and all trials were spaced out with at least an hour between runs, during which vacuum was applied to the chamber. Odors and injection treatments were given in counterbalanced, independent order within experimental groups.

Open field test

The open field is a square arena illuminated to 100-150 lux by ambient lighting. Mice were habituated to the room for at least an hour prior to testing, but otherwise had no prior experience in the arena prior to exposure. Mice were placed in the center of a square arena (27.3 × 27.3 ×

1388 20.3 cm, Med Associates) with four transparent plexiglass walls. Overall locomotion, immobility,
1389 and time spent in corners and center regions of arena during each epoch was analyzed for each
1390 mouse. Immobility was defined as movement under 0.5 cm/s for a period of at least 1 s, while
1391 the center was defined as the middle 13.7 × 13.7 cm square in the center of the arena and the
1392 corners as the corner regions that do not overlap with the center square in either direction (25%
1393 of arena area for each region). For optogenetic experiments, mice were allowed to move freely
1394 throughout the arena for 25 min total, with 5-8 mW 473 nm light stimulation pulsed with 50 ms
1395 bins at 20 Hz, alternately delivered during the 5-10 min and 15-20 min epochs (OFF, ON, OFF,
1396 ON, OFF). For chemogenetic experiments, mice were allowed to freely move through the area
1397 for 10 min total.

1398 ***Elevated plus maze***

1399 The arms of the elevated plus maze were 30.5 × 5.5 cm. The height of the closed arm walls was
1400 15 cm. The maze was elevated 40 cm from the floor and was placed in the center of the
1401 behavior room away from other stimuli. Arms were illuminated to 0-10 lux, with infrared
1402 illumination. Mice were placed in the center of maze at the beginning of each trial. For
1403 optogenetic experiments, mice were allowed to move freely throughout the maze for 15 min
1404 total, with 5-8 mW 473 nm light stimulation pulsed with 50 ms bins at 20 Hz delivered during the
1405 5-10 min epoch (OFF, ON, OFF). For chemogenetic experiments, mice were allowed to freely
1406 move through the area for 10 min total.

1407 **Histology**

1408 ***Section preparation***

1409 All sacrifices were performed during the dark period of the light cycle. Animals were
1410 anesthetized prior to sacrifice via combined intraperitoneal injection of 150 mg/kg ketamine
1411 (Zetamine, Vet One) and 15 mg/kg xylazine (AnaSed, AMRI Rensselaer). Except for animals
1412 used in sequencing studies, animals were subject to transcardial perfusion with 10 mL of sterile
1413 phosphate-buffered saline (PBS), followed by 10 mL 4% paraformaldehyde (PFA) solution. The
1414 brain was then extracted from the animal and placed into a 4% (PFA) solution in PBS for at
1415 least 36 hours until it was sectioned on a VT1000S vibratome (Leica). For tissue extracted for
1416 non-RNAscope histology, mice were transcardially perfused with 20 ml phosphate buffered
1417 saline (PBS) followed by 20 ml 4% paraformaldehyde (PFA) in PBS. All brains were extracted
1418 and post-fixed for at least 24 hours in 4% PFA. For tissue extracted for RNAscope, mice under
1419 6 months of age were decapitated once unconscious and their brains were extracted into a
1420 square Peel-A-Way embedding mold (Polysciences) and embedded in OCT (Fisher), and then
1421 snap-frozen a dry-ice/isopentane slurry and stored at -80˚C until cryosectioning within a month
1422 of sacrifice.

1423 Tissue was mounted in 5% agarose and sectioned sagittally on a vibratome for retrograde
1424 experiments, or sectioned coronally without mounting for all other non-RNAscope experiments.
1425 These sections were cut at 50 µm and stored in PBS before processing. All connectomic
1426 quantitation was performed on samples using epifluorescence without immunolabeling to avoid
1427 potential bias due to non-stoichiometric antibody binding, while all others were immunolabeled

1428 for visualization of viral targeting accuracy and collection of representative images.
1429 Immunolabeling of eYFP and other GFP-derived fluorophores was performed using goat anti-
1430 GFP primary antibodies (Abcam) and Alexa Fluor 488-conjugated anti-goat secondary
1431 antibodies (Invitrogen), while immunolabeling of mCherry and other DsRed-derived fluorophores
1432 used rabbit anti-DsRed primary antibodies (Takara) and Alexa Fluor 588-conjugated anti-rabbit
1433 antibodies (Invitrogen), all diluted 1:1000 in PBS-T. All non-RNAscope sections were mounted
1434 on Superfrost Plus microscope slides (Fisher) and counterstained with Fluoromount-G
1435 containing DAPI (SouthernBiotech). Sections were stored long-term at 4˚C.

1436 ***RNAscope fluorescence* in situ *hybridization***

1437 RNAscope sections were cut at 15 µm on a CM 1950 cryostat (Leica) and mounted on
1438 Superfrost Plus slides and stored at -80˚C until processing via RNAscope within a month of
1439 mounting. RNAscope was performed in an RNA-free environment according to manufacturer
1440 instructions using the Multiplex Fluorescent Reagent Kit v2 (Advanced Cell Diagnostics).
1441 RNAscope was performed using the probes *mm-Slc17a7* in the C2 channel, and *mm-Slc17a6* in
1442 the C3 channel, dyed with Opal 520 and Opal 690 in a counterbalanced manner at 1:15,000
1443 concentration to reduce background fluorescence and allow quantitation of unsaturated, clearly-
1444 distinguishable puncta. Processed RNAscope sections were then mounted with Prolong
1445 Antifade Diamond (ThermoFisher) and stored long-term at 4˚C.

1446 ***Fluorescence image acquisition***

1447 Non-RNAscope Images were acquired at 10X magnification with an VS120 slide scanner
1448 (Olympus), with settings held constant within experiments. Confocal fluorescence images for
1449 RNAscope were acquired on an SP8 (Leica) confocal laser scanning microscope using a
1450 40x/1.30NA oil immersion objective. Serial Z-stack images were acquired using the LASX
1451 software at a thickness of 1 µm per Z stack, with 14-21 planes taken per image. Images were
1452 acquired with identical settings for laser power, detector gain, and amplifier offset for each set of
1453 counterbalanced probe-fluorophore combinations.

1454 **Sequencing Data Acquisition**

1455 ***Tissue extraction and cryopreservation for single-cell sequencing***

1456 Once unconscious, mice animals were transcardially perfused with ice-cold, carbogen-bubbled
1457 (95% O2, 5% CO2), nuclease-free, 0.22 µm sterile-filtered artificial cerebrospinal fluid (ACSF)
1458 with a composition of 93 mM N-methyl-D-glucamine, 2.5 mM KCl, 1.2 mM NaH2PO4, 30 mM
1459 NaHCO3, 20 mM HEPES, 25 mM glucose, 5 mM sodium ascorbate, 2 mM thiourea, 3 mM
1460 sodium pyruvate, 13.2 mM trehalose, 12 mM N-acetyl-cysteine, 0.5 mM CaCl2, 10 mM MgSO4,
1461 and 93 mM HCl, at pH 7.3-7.4[31]. Following transcardial perfusion, brains were immediately
1462 extracted and submerged into ice-cold carbogen-bubbled ACSF, with less than 5 minutes
1463 between the beginning of perfusion and final submersion after extraction. Brains were serially
1464 sectioned in ice-cold, carbogen-bubbled ACSF on a VT1000S vibratome (Leica) with
1465 polytetrafluoroethane-coated razor blades (Ted Pella) at 0.15 mm/sec and 100 Hz, dividing the
1466 whole cerebrum into 400 µm coronal slices. Target regions were microdissected from these

1467 slices under a stereomicroscope using a sterile blunt-end needle (22 gauge for CeA, ASt, and
1468 tail of striatum, 16 gauge for dorsal striatum). All regions were targeted using Paxinos &
1469 Franklin, 5th Edition, as reference.[13] Extracted tissue samples were recovered in ice-cold,
1470 nuclease-free, 0.22 µm sterile-filtered cryoprotective nuclear storage buffer, composed of 0.32
1471 M sucrose, 5 mM CaCl2, 3 mM magnesium acetate, 10 mM Trizma hydrochloride buffer (pH
1472 8.0), 1 mM dithiothreitol, 0.02 U/µl SUPERase•In RNAse Inhibitor (Invitrogen), and 1X cOmplete
1473 Protease Inhibitor Cocktail with EDTA (Roche). Tissue was then snap frozen using a metal
1474 CoolRack M90 (Biocision) pre-chilled to -80˚C and stored at -80˚C until nuclear isolation.
1475 Following extraction of tissue regions of interest, remaining portions of sections were fixed in 4%
1476 paraformaldehyde and 4′,6-diamidino-2-phenylindole (DAPI) was applied to sections at 1 µg/ml.
1477 After fixation and staining, sections were mounted and imaged on an VS120 slide scanner
1478 (Olympus). From these images, dissection accuracy was assessed for each region, and
1479 individual samples were only selected for downstream nuclear isolation if the extracted tissue
1480 fell entirely within the defined target regions.

1481 Nuclear isolation procedures were adapted from multiple methods described previously[79,
1482 80].[14,15] All procedures were performed on ice, and all solutions were ice-cold, nuclease-free,
1483 and 0.22 µm sterile-filtered. Cryopreserved tissue pieces were slow thawed by incubation at 4˚C
1484 for 1 hour prior to isolation. Tissue pieces were then pooled and resuspended in nuclear
1485 isolation medium composed of 0.25 M sucrose, 25 mM KCl, 5 mM MgCl2, 10 mM Trizma
1486 hydrochloride buffer (pH 7.4), 1 mM dithiothreitol, 0.04 U/µl RNasin Plus RNAse Inhibitor
1487 (Promega), 1X cOmplete Protease Inhibitor Cocktail with EDTA (Roche), and 0.1% Triton-X.
1488 The pooled tissue pieces in nuclear isolation medium were transferred to a 2 mL Dounce tissue
1489 grinder. Tissue was homogenized by 5 strokes from the loose pestle and 15 followed by the
1490 tight pestle, and the resulting homogenate was filtered through a 40 µm Flowmi cell strainer
1491 (Bel-Art) into a 1.5 ml Lo-Bind tube (Eppendorf). The homogenate was then centrifuged with a
1492 swinging bucket rotor at 4˚C and 1000 x g for 8 minutes. Nuclei were then washed with nuclear
1493 flow buffer composed of DPBS with 1% bovine serum albumin, 1 mM dithiothreitol, and 0.04
1494 U/µl RNasin Plus RNAse Inhibitor (Promega) and centrifuged at 4˚C and 500 x g for 5 minutes,
1495 which was subsequently repeated. Nuclei were finally resuspended in nuclear flow buffer
1496 containing 3 µm DRAQ7 (Cell Signaling Technology) and again filtered through a 40 µm Flowmi
1497 cell strainer into a 5 ml round-bottom polystyrene tube. Each isolation took under 45 minutes to
1498 perform, from homogenization to final suspension.

1499 ***Fluorescence-activated nuclei sorting (FANS)***

1500 FANS was carried out on a FACSAria II SORP (BD Biosciences) using a 70 µm nozzle at 52
1501 PSI sheath pressure. For FANS, debris was first excluded by gating on forward and side scatter
1502 pulse area parameters (FSC-A and SSC-A), followed by exclusion of aggregates (FSC-W and
1503 SSC-W), and finally gating for nuclei based on DRAQ7 fluorescence (APC-Cy7). Nuclei were
1504 successively sorted into 1.5 ml LoBind tubes (Eppendorf) under the purity sort mode. The tube
1505 contained 10X RT master mix without RT Buffer C. 16,000 total nuclei were targeted for
1506 downstream processing, and to account for cytometer errors and subsequent loss of nuclei,
1507 21,000 were sorted into the tube. Nuclei were then immediately processed for snRNA-seq.
1508 FANS conditions were optimized for isolation of debris-free nuclei using the LIVE/DEAD

1509 Viability/Cytotoxicity Kit for Mammalian Cells (Molecular Probes), adding to the final suspension
1510 according to manufacturer instructions and examining on a hemocytometer using an EVOS FL
1511 Cell Imaging System (Thermo Fisher) for enrichment of ethidium homodimer-1-positive nuclei
1512 and the absence of Calcein AM-labeled cellular debris.

1513 ***Tissue extraction and sample preparation for spatial transcriptomics***

1514 Mice were euthanized with CO_2 followed by decapitation, either in the dark or in the light. Brain
1515 hemispheres were collected and placed in OCT and then flash frozen in isopentane in liquid
1516 nitrogen. One hemibrain from each mouse was cryosectioned at -18°C sagittally to a thickness
1517 of 10 mm (~2.8 mm from the midline) using a standard Leica CM1860 cryostat and processed
1518 according to the recommended protocols (Tissue optimization: CG000240 Visium 10X
1519 Genomics; Gene expression: CG000239). The tissue was immediately mounted on a Visium
1520 spatially barcoded slide (10X Genomics). The tissue was covered with OCT and kept at -80
1521 degrees C until it was cryosectioned again starting at the same position to a thickness of 10mm
1522 and mounted onto a Superfrost plus microscope slide (Fisherbrand) for staining. Each section
1523 covered approximately 80% of the 5,000 total spots within their fiducial frame. Slides were
1524 stored at -80˚C until use.

1525 **Library Preparation**

1526 ***Library preparation for single nucleus sequencing***

1527 Nuclear suspensions were converted into barcoded snRNA-seq libraries using the Chromium
1528 Next GEM Single Cell 3' v3.1 Reagent Kits v3.1 Single Index (10X Genomics). Library
1529 preparation for both assays was performed in accordance with the manufacturer's instructions.
1530 10,000 nuclei were targeted during each snRNA-seq library preparation run. 10X libraries were
1531 first sequenced at low depth on a NextSeq 550 Sequencing System (Illumina) to estimate
1532 quality and number of nuclei for each library, followed by deep sequencing on a NovaSeq 6000
1533 Sequencing System. All runs were performed using 2 x 100-bp paired-end reads, outputting
1534 data in 28/8/91-bp read format for snRNA-seq runs.

1535 ***Library preparation for Visium spatial transcriptomics***

1536 Tissue was harvested from 7 month old, non-transgenic littermates from a cross to an App23
1537 Alzheimer's model in a C57BL6/J background (Romero et al., in preparation). Visium spatial
1538 gene expression slides and reagents were used according to the manufacturer instructions (10X
1539 Genomics). Each capture area was 6.5mm x 6.5 mm and contained 5,000 barcoded spots that
1540 were 55 µm in diameter (100 µm center to center between spots) provide an average resolution
1541 of about 1 to 10 cells per spot. Optimal permeabilization time was measured at 24 min. Libraries
1542 were prepared according to the Visium protocol (10X Genomics) and sequenced on a
1543 NovaSeq4 (Illumina) at a sequencing depth of 182 million read pairs. Sequencing was
1544 performed with the recommended protocol in a 28/10/10/100-bp read format. H&E
1545 (Hematoxylin, Thermo; Dako bluing buffer, Dako; Eosin Y, Sigma) staining and image
1546 preparation was performed according to the Visium protocol. H&E-stained sections were

imaged using a Nanozoomer slide scanner (Hamamatsu) Spatial gene expression assay was performed according to the protocol CG000239.

QUANTIFICATION AND STATISTICAL ANALYSIS

Statistical Analysis

All statistical details can be found in the figure legends. Sample sizes for behavioral studies were chosen based on past optogenetic studies for each behavior, which had used 6-15 animals per group. Blinding experimenters was not possible for behavioral, imaging, or sequencing experiments, given familiarity with subjects, but manual quantitation for connectivity experiments was performed blinded to group with random assignment. All statistical tests were performed in R (v4.2.3) unless otherwise specified. All statistical tests were performed with two tails. Group comparisons were made using two-way analysis of variance (ANOVA) followed by Bonferroni post hoc tests, except where otherwise specified. All behavioral experiments were performed by multiple experimenters across multiple cohorts each composed of multiple litters, with littermates distributed across control and treatment groups, with all such cohorts yielding similar results (data not shown), and topography stimulation experiments were performed across multiple facilities and institutions. Numbers of mice used for all non-sequencing experiments are reported within the relevant figures, figure legends, and the text.

Calcium Imaging Data Analysis

Image processing

Data analysis for calcium imaging experiments was adapted from methods previously described[20]. Ca^{2+} imaging data were first motion-corrected using the non-rigid motion correction algorithm NoRMCorre[81]. Afterwards, neural traces were extracted from the motion-corrected data using constrained nonnegative matrix factorization (CNMF)[82]. Spatial components identified by CNMF were inspected by eye to ensure they were not artifacts. A Gaussian Mixture Model (GMM) was used to estimate the baseline fluorescence of each neuron. To account for potential low-frequency drift in the baseline, the GMM was applied along a moving window of 2,500 frames (500 seconds). The fluorescence of each neuron at each time point t was then normalized to the moving baseline to calculate $\Delta F/F = F_t - F_{baseline} / F_{baseline}$. All subsequent analysis was performed using custom code written in MATLAB (R2022b).

Hierarchical clustering of pooled averaged responses

ΔF/F in response to all 6 odors were averaged across trials then Z-scored. The resulting trial-average values from the following time bins were averaged across time: the first second during each odor, the last second during each odor, and the first second after each odor. The resulting 18-element vectors were sorted into 6 clusters after agglomerative hierarchical clustering using Euclidean distance and Ward linkage.

Responsiveness criteria

To determine how many neurons were responsive to a given odor, we compared ΔF/F at each frame during the 2 second odor period against a pooled distribution of ΔF/F values from the 2-seconds prior to odor onset using a Wilcoxon rank sum test. The resulting p-values were evaluated with Holm-Bonferroni correction to ensure that familywise error rate (FWER) was below 0.05. We also counted the number of neurons that were significantly responsive for at least 4 frames during the odor period to report the total percentage of responsive neurons during odor.

Single-neuron 6-odor classifiers

To test how reliably a single neuron's fluorescence could discriminate between the 6 odors, we assessed the performance of multinomial regression (MNR) classifiers trained on a single neuron's responses to 6 odors. For each neuron and odor pair, we averaged the ΔF/F during the last second of the odor exposure for each trial then Z-scored across all trials. The last second was used because classifier performance is highest during the last second of odor exposure and the first second after odor offset. The resulting feature vector, a single dimensional vector of length 120 (6 odors x 20 trials), was used to train the MNR classifiers. The 5-fold cross-validated accuracies are reported and plotted as violin plots. As a control for each neuron, 100 shuffled classifiers were trained on the data with the odor labels randomly assigned.

Pairwise euclidean distance

To quantify the differences among population-level responses to the 6 odors, we quantified the pairwise Euclidean distance between the trajectories of odor responses. First, we subtracted the ΔF/F values during the 2 seconds prior to odor delivery from each frame then averaged these values across trials for each odor. The pairwise Euclidean distance at each frame was computed for each odor pair and normalized to the maximum pairwise distance measured in all odor pairs at any time bin. These calculations were carried out separately for each animal and then averaged across biological replicates to report the mean and the standard error.

Population classifiers

To assess the discriminability of odor responses in high-dimensional space, we measured the accuracy of error-correcting output codes (ecoc) classifiers. At each time point relative to odor delivery, we pooled ΔF/F values from all trials during which either odor was presented. The feature vector is a multidimensional vector of length 120 (6 odors x 20 trials) and varying width k between 1 and 300. These values were then normalized and used to train a multinomial ecoc classifier using a Support Vector Machine (SVM). The accuracy of the classifier was evaluated via 5-fold cross-validation. To compare the classifier accuracies across different numbers of neurons used for training, we randomly selected varying numbers of pooled neurons and used the ΔF/F values during the last second of odor exposure for training.

Behavioral Data Analysis

Behavioral metrics (i.e. performance index, port distance, center distance, open field time, and total distance) for the four-quadrant preference test, open field test, and elevated plus maze were calculated on sets of coordinates created by identifying the centroid of the mouse in real time in video collected from an overhead camera (Basler) at 4 Hz using custom Labview code and outputting the centroid's coordinates for each frame. The mouse was automatically identified by taking a background greyscale image of the behavioral assay's environment at the beginning of each trial and detecting shapes of a minimum size deviating from the background image by a specific threshold. The centroid was then determined by automated generation of a bounding box for the mouse in each frame in real time and recording the coordinate of the centroid of this rectangle.

Four quadrant task data analysis

Mice were tested as previously described[14]. Mice were placed in the chamber for 25 min experiments and tested no more than once per day. The first 10 min served as a baseline test for spatial or temporal bias within the chamber during the trial, and no stimulus of any sort was provided, while the last 15 min were the test of the manipulation. 15 minutes was chosen to balance time courses of odor responses observed in previous experiments, where appetitive odors tend to yield initial responses that decay, while aversive odors tend to yield responses that grow in magnitude over time. To ensure effects did not arise from ceiling or floor effects in the baseline or from a nonstandard baseline internal state, the mouse had to remain within the stimulus quadrant during the baseline test between ~20-30% of the time or else the experiment was terminated, and the mouse was tested again later. The first 2 minutes of data after the stimulus was introduced were excluded from the analysis to reduce variance and account for novelty of the stimulus without affecting the overall valence of the behavioral response, and the last minute of data was excluded to ensure no minor differences in frames captured could affect analysis. For chemogenetic odor response silencing experiments, animals with responses below an absolute value of 0.1 during saline trials, were excluded from experiments to avoid false negatives from attempting to silence a response that was not observed at baseline, which applied to less than a quarter of overall animals tested across experimental conditions. Performance index represents the percent difference from chance occupancy in the manipulation quadrant, calculated as $PI = (P - 0.25) / 0.25$; where P is the fraction of time the animal spends in the manipulation quadrant. Mean port distance represents the mean distance of each point to the deepest point into the manipulation quadrant observed at baseline.

Open field test data analysis

For elevated plus maze analysis, all chemogenetic inhibition trials used the entirely of the 10 min test length as a single period, while optogenetic stimulation trials used the mean of the three "OFF" periods to compare to the mean of the two "ON" periods. Three metrics of interest were calculated. Center time was calculated as the proportion of time spent in the middle square of the open field comprising 50% of its total area. Corner time was calculated as the proportion of time spent in the corner squares bounded by the walls and the lines bounding the center region. Time immobile was calculated as the proportion of time when the animal moved less than 1 cm/s for at least a one-second period. Location of the open field and bounding

regions was kept constant from trial to trial by registering the apparatus to a bounding box with the same top-down dimensions, and every measured centroid outside of the registered region resulting from shadows cast and other artifacts was interpolated between the closest points before and after within the region.

Elevated plus maze data analysis

For elevated plus maze analysis, all chemogenetic inhibition trials used the entirely of the 10 min test length as a single period, while optogenetic stimulation trials used the mean of the two “OFF” periods to compare to the “ON” period. Three metrics of interest were calculated. Time in the open arms was calculated as the proportion of time spent in the open arms compared to the whole period of interest and did not include time in the center between the two arms. Open arm entries measures number of episodes where the centroid is observed outside of the bounds of the closed arms or the center region, without any minimum time or distance out onto the open arms. Finally, distance was simply calculated as the distance traveled during each period of interest. Location of open and closed arms was kept constant from trial to trial by registering the apparatus to a cross-shaped bounding box with the same top-down dimensions, and every measured centroid outside of the registered region due to factors like the mouse leaning over the edge of the open arms, among others, was interpolated between the closest points before and after within the region.

Analysis of Single-Nucleus RNA Sequencing Data

Sequence alignment

All samples were processed using Cell Ranger (v5.0.0)[83]. All processing was done by using Cell Ranger's implementation of STAR to align sample sequence reads to their pre-built mm10 vm23/Ens98 reference transcriptome index 2020-A, with predicted and non-validated transcripts removed. All sequencing reads were aligned to both the exons and the introns present in the index. Samples were demultiplexed to produce a pair of FASTQ files for each sample. FASTQ files containing raw read sequence information were aligned to the Cell Ranger index using the cellranger count command with --chemistry SC3Pv3 and --include-introns flags enabled. Cell Ranger corrected sequencing errors in cell barcodes to pre-defined sequences in the 10X v3 single-index whitelist within Hamming distance 1. PCR duplicates were removed by selecting unique combinations of corrected cell barcodes, unique molecular identifiers, gene names, and location within the transcript. Raw unfiltered count data was read into R (v4.2.1) using the Seurat package (v4.2.0)[84]. The final result of the pipeline was a barcode x gene expression matrix for further analysis downstream.

Quality control

We used the raw, unfiltered matrix output from Cell Ranger as the input to the beginning of the pipeline. However, to apply a more stringent filter, the emptyDrops dirichlet-multinomial model from the DropletUtils package (v1.10.2) was applied to each library individually. Droplets with less than 100 total counts were used to construct the ambient RNA profile and an FDR threshold below 0.001 was used to select putatively occupied droplets. All barcodes with greater

1700 than 1000 UMIs were further assumed non-empty. Most quality filtration choices were heavily
1701 influenced by the recommendations presented in pipeComp[85]. All quality control was
1702 performed on each library individually prior to merging. Minimal quality filtering for each barcode
1703 was performed by setting a floor of 1000 features per barcode for downstream inclusion to
1704 ensure the dataset is entirely composed of high-quality nuclei. Next, to remove highly likely
1705 multiplet barcodes, barcodes were filtered out if their count depth was more than 5 median
1706 absolute deviations above the median count depth. Barcodes were then removed if their
1707 proportion of ribosomal or mitochondrial reads was more than 5 interquartile ranges above the
1708 75th percentile (median absolute deviations cannot be used, because in many cases the
1709 median absolute deviation is 0). Heterotypic doublets were identified by creating simulated
1710 artificial doublets in scDblFinder (v1.4.1), which uses a DoubletFinder-like model to remove
1711 barcodes similar to simulated doublets, with an assumed doublet rate of 1% per 1000 nuclei in
1712 the library[86]. Scater (v1.18.3) was used to produce initial diagnostic tSNE and UMAP plots for
1713 visually checking the influence of each above metric on the structure of the data[87].

1714 ***Data processing/transformation***

1715 All datasets (initially for all nuclei and again for selected subclusters) were formatted into Seurat
1716 objects (v4.0.0), merged, and then normalized and transformed individually using the
1717 SCTransform (v2) variance stabilizing transform, which performs best according to prior
1718 comparisons in pipeComp[85]. Following the merge, all genes expressed in 3 or fewer nuclei of
1719 interest were removed from analysis. SCTransform was run returning Pearson residuals
1720 regressing out mitochondrial gene expression, retaining the top 5000 highly variable features.
1721 Dimensionality of the dataset was first reduced using principal component analysis, as
1722 implemented in Seurat's RunPCA function, retaining the top 50 principal components. Principal
1723 components were selected for downstream use by using the lower value of either the number of
1724 principal components where the lowest contributes 5% of standard deviation and all
1725 cumulatively contribute 90% of the standard deviation, or the number of principal components
1726 where the percent change in variation between the consecutive components is lower than 0.1%.
1727 These principal components were used as input to the non-linear tSNE and UMAP
1728 dimensionality reduction methods as implemented by Seurat's RunTSNE and/or RunUMAP
1729 functions with 1000 epochs at 0.5 minimum distance, with otherwise default settings.

1730 Clusters were identified via Leiden clustering in latent space using the previously selected
1731 principal components as input. Optimal clustering resolution was identified in a supervised
1732 manner using clustree, finding the highest resolution for each dataset where clustering remains
1733 stable[88]. Cluster annotation was performed in a semi-hierarchical semi-supervised manner,
1734 where known marker genes were first used to separate all nuclei into neuronal and non-
1735 neuronal cell types, and then these cells were re-analyzed and neurons were respectively
1736 separated into glutamatergic and GABAergic neurons, while non-neuronal cells were separated
1737 into astrocytes, microglia, macrophages, oligodendrocytes and their precursors/lineage, mural
1738 cells, endothelia, and vascular leptomeningeal cells. This lower level of cells was then
1739 reanalyzed, and novel cell types were then identified within these more-granular known cell
1740 types. For identification of known cell types, clusters expressing the same marker genes were
1741 manually merged to ensure all cells of a known type were analyzed together, which did not

occur for novel cell type identification. Clusters resulting from specific difference in nuclei quality instead of true changes in gene expression (i.e. markedly lower mean UMI/features per nucleus, increased ribosomal/mitochondrial gene expression proportion) were removed prior to final clustering. Relationships between cell type proportion and plCoA zone were quantitated using propeller, treating each library as an independent replicate[89].

Differential expression

Marker genes were identified using Wilcoxon rank-sum test as implemented by the FindConservedMarkers function in Seurat, using the region as a grouping variable. Genes were accepted as differentially expressed with a minimum proportion cutoff at 0.1 and minimum fold change at 1.5-fold (log2-fold change of 0.585), with a p-value cutoff of 0.01 after Bonferroni correction. To identify genes differentially expressed by region, single-cell values were converted to pseudo-bulk by batch using the run_de function as implemented in the Libra package (v1.0.0) using default settings with a minimum proportion cutoff at 0.1, and tested for differential expression using edgeR’s likelihood ratio test. Zone-specific gene expression was identified by comparing batches from the two isolated zones.

Analysis of Spatial Transcriptomics Data

Sequence and image alignment

All samples were processed using Space Ranger (v1.3.0). All processing was done by using Space Ranger's implementation of STAR to align sample sequence reads to their pre-built mm10 vm23/Ens98 reference transcriptome index 2020-A, with predicted and non-validated transcripts removed, as in snRNA-seq data alignment. Samples were demultiplexed to produce a pair of FASTQ files for each sample. FASTQ files containing raw read sequence information were aligned to the index using the spaceranger count command. Space Ranger corrected sequencing errors in cell barcodes to pre-defined sequences in the single-index whitelist within Hamming distance 1. PCR duplicates were removed by selecting unique combinations of corrected cell barcodes, unique molecular identifiers, gene names, and location within the transcript. Imaging data was processed using automatic fiducial alignment and tissue detection on a brightfield input.

Data processing/transformation

We used the image-filtered matrix output from Space Ranger as the input to the beginning of the pipeline. In a similar manner to snRNA-seq data, all datasets were formatted into Seurat objects (v5.0.0), merged, and then normalized and transformed using the SCTransform (v2) variance stabilizing transform. SCTransform was run returning Pearson residuals regressing out mitochondrial gene expression, retaining the top 5000 highly variable features. Dimensionality of the dataset was first reduced using principal component analysis, as implemented in Seurat's RunPCA function, retaining the top 50 principal components, all of which were used in downstream processing. These principal components were used as input to the non-linear tSNE and UMAP dimensionality reduction methods as implemented by Seurat's RunTSNE and/or RunUMAP functions with 1000 epochs at 0.2 minimum distance, with otherwise default settings.

Clusters were identified via Leiden clustering in latent space using all 50 principal components as input. Optimal clustering resolution was identified in a supervised manner using clustree, finding the highest resolution for each dataset where clustering remains stable, choosing a resolution of 0.7. Cluster annotation was performed in a semi-supervised manner, observing where in captured plCoA regions each cluster's spots localized to. For clusters that could not be annotated from spatial location alone (e.g. OLG), marker genes were examined to determine the molecular identity of relevant spots. Spatial data was projected onto neuronal molecular cell types from snRNA-seq data and cell type likelihood was predicted using Seurat's FindTransferAnchors and TransferData functions using snRNA-seq data as a reference and plCoA spatial data as the query, using all 50 PCs. Prediction of a minority of subtypes failed, likely due to low abundance in tissue and/or due to mediolateral spatial differences, alluded to in a separate study, causing the section not to intersect with the part of the tissue containing the relevant neuronal subtypes. Glutamatergic and GABAergic molecular subtype likelihoods were predicted separately to remove noise and increase modeled prediction confidence.

Histological Image Analysis

Registration and localization

Histology for all animals and samples was examined prior to inclusion. Localization within the coronal plane was determined by registering the coronal slice to the Allen Brain Atlas via the ABBA plugin, using elastix to sequentially perform affine and spline registration of the DAPI channel of the slice to the Nissl channel of the atlas. The region of interest was then compared to the Paxinos and Franklin atlas to confirm localization, and find the region's anteroposterior distance from bregma. This combined method was used because sections cannot be accurately registered to the Paxinos and Franklin atlas due to low Z-resolution, while the Allen Brain Atlas lacks information about anteroposterior distance from bregma. Exclusion based on histology would occur when most of the intervention fell outside of the region of interest. Due to these differences, individual representative images use the individually registered Allen Reference Atlas schematics with the comparable Paxinos and Franklin anteroposterior coordinates noted, while consolidated targeting schematics use the Paxinos and Franklin atlas for visualization.

Quantification of histological fluorescence

In anterograde tracing experiments, output quantification was performed based on background-corrected total fluorescence. For all non-collateralization anterograde experiments, fluorescence intensities were quantified using FIJI (v2.9.0) throughout the whole brain in a series of evenly-space 50 μm coronal sections, manually segmenting by region with all settings held constant within experiments. For collateralization experiments, we exclusively examined fluorescence in the MeA and NAc. We calculated background-corrected total fluorescence using the equation $F_{total} = ID - (Area \times F_{background})$, where F_{total} is the background-corrected total fluorescence, ID is the integrated density, and $F_{background}$ is the mean background fluorescence measured from four randomly selected areas per section not receiving input from plCoA. Overall proportion was calculated by taking the sum of background-corrected fluorescence values across all sections for a given region and dividing it by the sum of all background-corrected values. For retrograde

experiments, we quantified number of cells using the Cell Counter plugin (v3.0.0) in FIJI. The sagittal brain slices containing the plCoA were then compared to Paxinos and Franklin, 5th Edition to count the number of cells found per distance away from bregma from -1.3 to -2.5 mm in increments of 100 µm. At least two sections per region per animal were analyzed. Representative images were produced from slide scanner image output, with background subtraction and uniform brightness and contrast thresholds applied equally to all fluorescent channels in FIJI to avoid potential distortion of visible fluorescence levels.

Quantification and analysis of RNAscope images

RNAscope images were analyzed as previously described.[16] Images were opened in FIJI and individual Z-planes encompassing the entire ROI were selected from each image for further image processing. Background was subtracted from all channels in all images using the subtract background feature. Masks of each region were drawn based on the mouse brain atlas, and images were then saved as 8bit TIFFs for further cell and puncta identification in CellProfiler (v4.2.4)[90]. Image TIFFs were run through CellProfiler using an optimized version of the CellProfiler Colocalization pipeline. The pipeline was optimized to identify DAPI labelled cells (15-45 pixels in diameter) and then subsequently identify mRNA puncta (4-10 pixels in diameter). DAPI cell detection was further restricted by shrinking DAPI ROIs by 1 pixel. Puncta overlapping with DAPI-identified cells (using the relate objects module) were considered for analysis to assess the level of mRNA expression per cell. To determine if cells were expressing mRNA, a threshold of 5 or more puncta within twice the diameter of nucleus centered over the nucleus was used. Total number and density of *VGluT2*+ and *VGluT1*+ cells in each region of interest were calculated from CellProfiler .csv outputs using custom R scripts.

1843 **References**

1844 1. Stowers, L., P. Cameron, and J.A. Keller, *Ominous odors: olfactory control of instinctive*
1845 *fear and aggression in mice.* Curr Opin Neurobiol, 2013. **23**(3): p. 339-45.
1846 2. Li, Q. and S.D. Liberles, *Aversion and Attraction through Olfaction.* Current Biology,
1847 2015. **25**(3): p. R120-R129.
1848 3. Hayden, S., et al., *Ecological adaptation determines functional mammalian olfactory*
1849 *subgenomes.* Genome Research, 2010. **20**(1): p. 1-9.
1850 4. Saraiva, L.R., et al., *A transcriptomic atlas of mammalian olfactory mucosae reveals an*
1851 *evolutionary influence on food odor detection in humans.* Science Advances, 2019. **5**(7):
1852 p. eaax0396.
1853 5. Ibarra-Soria, X., et al., *Variation in olfactory neuron repertoires is genetically controlled*
1854 *and environmentally modulated.* eLife, 2017. **6**: p. e21476.
1855 6. Yeshurun, Y. and N. Sobel, *An odor is not worth a thousand words: from*
1856 *multidimensional odors to unidimensional odor objects.* Annu Rev Psychol, 2010. **61**: p.
1857 219-41, C1-5.
1858 7. Tye, K.M., *Neural Circuit Motifs in Valence Processing.* Neuron, 2018. **100**(2): p. 436-
1859 452.
1860 8. Dewan, A., et al., *Non-redundant coding of aversive odours in the main olfactory*
1861 *pathway.* Nature, 2013. **497**(7450): p. 486-489.
1862 9. Saito, H., et al., *Immobility responses are induced by photoactivation of single*
1863 *glomerular species responsive to fox odour TMT.* Nature Communications, 2017. **8**(1): p.
1864 1-10.
1865 10. Semmelhack, J.L. and J.W. Wang, *Select Drosophila glomeruli mediate innate olfactory*
1866 *attraction and aversion.* Nature, 2009. **459**(7244): p. 218-23.
1867 11. Beyeler, A., et al., *Organization of Valence-Encoding and Projection-Defined Neurons in*
1868 *the Basolateral Amygdala.* Cell Reports, 2018. **22**(4): p. 905-918.
1869 12. Sosulski, D.L., et al., *Distinct representations of olfactory information in different*
1870 *cortical centres.* Nature, 2011. **472**(7342): p. 213-219.
1871 13. Miyamichi, K., et al., *Cortical representations of olfactory input by trans-synaptic*
1872 *tracing.* Nature, 2011. **472**(7342): p. 191-199.
1873 14. Root, C.M., C.A. Denny, R. Hen, and R. Axel, *The participation of cortical amygdala in*
1874 *innate, odour-driven behaviour.* Nature, 2014. **515**(7526): p. 269-73.
1875 15. Iurilli, G. and S.R. Datta, *Population Coding in an Innately Relevant Olfactory Area.*
1876 Neuron, 2017. **93**(5): p. 1180-1197 e7.
1877 16. Tsuji, T., et al., *Coding of odors in the anterior olfactory nucleus.* Physiological Reports,
1878 2019. **7**(22): p. e14284.
1879 17. Malnic, B., J. Hirono, T. Sato, and L.B. Buck, *Combinatorial receptor codes for odors.*
1880 Cell, 1999. **96**(5): p. 713-23.
1881 18. Stettler, D.D. and R. Axel, *Representations of odor in the piriform cortex.* Neuron, 2009.
1882 **63**(6): p. 854-64.
1883 19. Soucy, E.R., et al., *Precision and diversity in an odor map on the olfactory bulb.* Nature
1884 Neuroscience, 2009. **12**(2): p. 210-220.
1885 20. Lee, D., L. Liu, and C.M. Root, *Transformation of value signaling in a striatopallidal*
1886 *circuit.* eLife, 2023. **12**.

1887 21. Cousens, G.A., *Characterization of odor-evoked neural activity in the olfactory peduncle.*
1888 IBRO Reports, 2020. **9**: p. 157-163.
1889 22. Kim, J., et al., *Antagonistic negative and positive neurons of the basolateral amygdala.*
1890 Nat Neurosci, 2016. **19**(12): p. 1636-1646.
1891 23. Chen, X., et al., *A Gustotopic Map of Taste Qualities in the Mammalian Brain.* Science
1892 (New York, N.Y.), 2011. **333**(6047): p. 1262-1266.
1893 24. Kobayakawa, K., et al., *Innate versus learned odour processing in the mouse olfactory*
1894 *bulb.* Nature, 2007. **450**(7169): p. 503-8.
1895 25. Wang, L., et al., *The coding of valence and identity in the mammalian taste system.*
1896 Nature, 2018. **558**(7708): p. 127-131.
1897 26. Boyden, E.S., et al., *Millisecond-timescale, genetically targeted optical control of neural*
1898 *activity.* Nat Neurosci, 2005. **8**(9): p. 1263-8.
1899 27. Tasic, B., et al., *Adult mouse cortical cell taxonomy revealed by single cell*
1900 *transcriptomics.* Nat Neurosci, 2016. **19**(2): p. 335-46.
1901 28. Zeisel, A., et al., *Molecular Architecture of the Mouse Nervous System.* Cell, 2018.
1902 **174**(4): p. 999-1014 e22.
1903 29. Marques, S., et al., *Oligodendrocyte heterogeneity in the mouse juvenile and adult*
1904 *central nervous system.* Science (New York, N.Y.), 2016. **352**(6291): p. 1326-1329.
1905 30. Yasuda, K., et al., *Drug Transporters on Arachnoid Barrier Cells Contribute to the*
1906 *Blood–Cerebrospinal Fluid Barrier.* Drug Metabolism and Disposition, 2013. **41**(4): p.
1907 923-931.
1908 31. Tasic, B., et al., *Shared and distinct transcriptomic cell types across neocortical areas.*
1909 Nature, 2018. **563**(7729): p. 72-78.
1910 32. Yao, Z., et al., *A taxonomy of transcriptomic cell types across the isocortex and*
1911 *hippocampal formation.* Cell, 2021. **184**(12): p. 3222.
1912 33. Armbruster, B.N., et al., *Evolving the lock to fit the key to create a family of G protein-*
1913 *coupled receptors potently activated by an inert ligand.* Proc Natl Acad Sci U S A, 2007.
1914 **104**(12): p. 5163-8.
1915 34. Muller, M. and M. Fendt, *Temporary inactivation of the medial and basolateral*
1916 *amygdala differentially affects TMT-induced fear behavior in rats.* Behav Brain Res,
1917 2006. **167**(1): p. 57-62.
1918 35. Ikemoto, S., *Dopamine reward circuitry: two projection systems from the ventral*
1919 *midbrain to the nucleus accumbens-olfactory tubercle complex.* Brain Research Reviews,
1920 2007. **56**(1): p. 27-78.
1921 36. Kaas, J.H., *Topographic maps are fundamental to sensory processing.* Brain Res Bull,
1922 1997. **44**(2): p. 107-12.
1923 37. Garrett, M.E., I. Nauhaus, J.H. Marshel, and E.M. Callaway, *Topography and Areal*
1924 *Organization of Mouse Visual Cortex.* Journal of Neuroscience, 2014. **34**(37): p. 12587-
1925 12600.
1926 38. Kaas, J.H., et al., *Multiple Representations of the Body Within the Primary*
1927 *Somatosensory Cortex of Primates.* Science, 1979. **204**(4392): p. 521-523.
1928 39. Schreiner, C.E. and J.A. Winer, *Auditory Cortex Mapmaking: Principles, Projections,*
1929 *and Plasticity.* Neuron, 2007. **56**(2): p. 356-365.
1930 40. Miyamichi, K., et al., *Cortical representations of olfactory input by trans-synaptic*
1931 *tracing.* Nature, 2011. **472**(7342): p. 191-6.

41. Wang, I.H., et al., *Spatial transcriptomic reconstruction of the mouse olfactory glomerular map suggests principles of odor processing.* Nature Neuroscience, 2022. **25**(4): p. 484-492.
42. Ressler, K.J., S.L. Sullivan, and L.B. Buck, *A zonal organization of odorant receptor gene expression in the olfactory epithelium.* Cell, 1993. **73**(3): p. 597-609.
43. Zapiec, B. and P. Mombaerts, *The Zonal Organization of Odorant Receptor Gene Choice in the Main Olfactory Epithelium of the Mouse.* Cell Reports, 2020. **30**(12): p. 4220-4234.e5.
44. Kermen, F., et al., *Topographical representation of odor hedonics in the olfactory bulb.* Nature Neuroscience, 2016. **19**(7): p. 876-878.
45. Choi, G.B., et al., *Lhx6 Delineates a Pathway Mediating Innate Reproductive Behaviors from the Amygdala to the Hypothalamus.* Neuron, 2005. **46**(4): p. 647-660.
46. Cohn, R., I. Morantte, and V. Ruta, *Coordinated and Compartmentalized Neuromodulation Shapes Sensory Processing in Drosophila.* Cell, 2015. **163**(7): p. 1742-1755.
47. Chen, K., J.F. Kogan, and A. Fontanini, *Spatially Distributed Representation of Taste Quality in the Gustatory Insular Cortex of Behaving Mice.* Current Biology, 2021. **31**(2): p. 247-256.e4.
48. Erö, C., M.-O. Gewaltig, D. Keller, and H. Markram, *A Cell Atlas for the Mouse Brain.* Frontiers in Neuroinformatics, 2018. **12**.
49. Cembrowski, M.S., et al., *Dissociable Structural and Functional Hippocampal Outputs via Distinct Subiculum Cell Classes.* Cell, 2018. **173**(5): p. 1280-1292.e18.
50. Cembrowski, M.S. and N. Spruston, *Heterogeneity within classical cell types is the rule: lessons from hippocampal pyramidal neurons.* Nature Reviews Neuroscience, 2019. **20**(4): p. 193-204.
51. Scala, F., et al., *Phenotypic variation of transcriptomic cell types in mouse motor cortex.* Nature, 2021. **598**(7879): p. 144-150.
52. Calvigioni, D., et al., *Esr1+ hypothalamic-habenula neurons shape aversive states.* Nature Neuroscience, 2023. **26**(7): p. 1245-1255.
53. Phillips, J.W., et al., *A repeated molecular architecture across thalamic pathways.* Nature neuroscience, 2019. **22**(11): p. 1925.
54. Mandelbaum, G., et al., *Distinct Cortical-Thalamic-Striatal Circuits through the Parafascicular Nucleus.* Neuron, 2019. **102**(3): p. 636-652.e7.
55. Hochgerner, H., et al., *Neuronal types in the mouse amygdala and their transcriptional response to fear conditioning.* Nature Neuroscience, 2023. **26**(12): p. 2237-2249.
56. Klingler, E., *Development and Organization of the Evolutionarily Conserved Three-Layered Olfactory Cortex.* eNeuro, 2017. **4**(1).
57. Shi, H., et al., *Spatial atlas of the mouse central nervous system at molecular resolution.* Nature, 2023. **622**(7983): p. 552-561.
58. Yao, Z., et al., *A high-resolution transcriptomic and spatial atlas of cell types in the whole mouse brain.* Nature, 2023. **624**(7991): p. 317-332.
59. Zhang, M., et al., *Molecularly defined and spatially resolved cell atlas of the whole mouse brain.* Nature, 2023. **624**(7991): p. 343-354.
60. Mills, F., et al., *Amygdalostriatal transition zone neurons encode sustained valence to direct conditioned behaviors*. 2022, bioRxiv.

61. Singer, W., *Recurrent dynamics in the cerebral cortex: Integration of sensory evidence with stored knowledge.* Proceedings of the National Academy of Sciences, 2021. **118**(33): p. e2101043118.
62. Floresco, S.B., *The Nucleus Accumbens: An Interface Between Cognition, Emotion, and Action.* https://doi.org/10.1146/annurev-psych-010213-115159, 2015.
63. Day, H.E., C.V. Masini, and S. Campeau, *The pattern of brain c-fos mRNA induced by a component of fox odor, 2,5-dihydro-2,4,5-trimethylthiazoline (TMT), in rats, suggests both systemic and processive stress characteristics.* Brain Res, 2004. **1025**(1-2): p. 139-51.
64. Zador, A.M., *A critique of pure learning and what artificial neural networks can learn from animal brains.* Nature Communications, 2019. **10**(1): p. 3770.
65. Koulakov, A., S. Shuvaev, D. Lachi, and A. Zador, *Encoding innate ability through a genomic bottleneck.* 2022, bioRxiv.
66. Barabási, D.L., T. Beynon, Á. Katona, and N. Perez-Nieves, *Complex computation from developmental priors.* Nature Communications, 2023. **14**: p. 2226.
67. Chae, H., et al., *Mosaic representations of odors in the input and output layers of the mouse olfactory bulb.* Nature Neuroscience, 2019. **22**(8): p. 1306-1317.
68. Martiros, N., V. Kapoor, S.E. Kim, and V.N. Murthy, *Distinct representation of cue-outcome association by D1 and D2 neurons in the ventral striatum's olfactory tubercle.* eLife, 2022. **11**: p. e75463.
69. Qiu, Q., Y. Wu, L. Ma, and C.R. Yu, *Encoding innately recognized odors via a generalized population code.* Current Biology, 2021. **31**(9): p. 1813-1825.e4.
70. Nair, A., et al., *An approximate line attractor in the hypothalamus encodes an aggressive state.* Cell, 2023. **186**(1): p. 178-193 e15.
71. Wang, Y., et al., *Large-scale forward genetics screening identifies Trpa1 as a chemosensor for predator odor-evoked innate fear behaviors.* Nat Commun, 2018. **9**(1): p. 2041.
72. Hacquemand, R., L. Jacquot, and G. Brand, *Comparative Fear-Related Behaviors to Predator Odors (TMT and Natural Fox Feces) before and after Intranasal ZnSO(4) Treatment in Mice.* Front Behav Neurosci, 2010. **4**: p. 188.
73. Ayers, L.W., A. Asok, F.D. Heyward, and J.B. Rosen, *Freezing to the predator odor 2,4,5 dihydro 2,5 trimethylthiazoline (TMT) is disrupted by olfactory bulb removal but not trigeminal deafferentation.* Behav Brain Res, 2013. **253**: p. 54-9.
74. Lin, P.A., S.K. Asinof, N.J. Edwards, and J.S. Isaacson, *Arousal regulates frequency tuning in primary auditory cortex.* Proc Natl Acad Sci U S A, 2019. **116**(50): p. 25304-25310.
75. Fanselow, E.E. and M.A. Nicolelis, *Behavioral modulation of tactile responses in the rat somatosensory system.* J Neurosci, 1999. **19**(17): p. 7603-16.
76. Fu, Y., et al., *A cortical circuit for gain control by behavioral state.* Cell, 2014. **156**(6): p. 1139-1152.
77. Davis, A., R. Gao, and N.E. Navin, *SCOPIT: sample size calculations for single-cell sequencing experiments.* BMC Bioinformatics, 2019. **20**(1): p. 566.
78. Sturchler-Pierrat, C., et al., *Two amyloid precursor protein transgenic mouse models with Alzheimer disease-like pathology.* Proceedings of the National Academy of Sciences, 1997. **94**(24): p. 13287-13292.

2022 79. Preissl, S., et al., *Single-nucleus analysis of accessible chromatin in developing mouse*
2023 *forebrain reveals cell-type-specific transcriptional regulation.* Nat Neurosci, 2018. **21**(3):
2024 p. 432-439.
2025 80. Krishnaswami, S.R., et al., *Using single nuclei for RNA-seq to capture the transcriptome*
2026 *of postmortem neurons.* Nat Protoc, 2016. **11**(3): p. 499-524.
2027 81. Pnevmatikakis, E.A. and A. Giovannucci, *NoRMCorre: An online algorithm for*
2028 *piecewise rigid motion correction of calcium imaging data.* Journal of Neuroscience
2029 Methods, 2017. **291**: p. 83-94.
2030 82. Pnevmatikakis, E.A., et al., *Simultaneous Denoising, Deconvolution, and Demixing of*
2031 *Calcium Imaging Data.* Neuron, 2016. **89**(2): p. 285-299.
2032 83. Zheng, G.X., et al., *Massively parallel digital transcriptional profiling of single cells.* Nat
2033 Commun, 2017. **8**: p. 14049.
2034 84. Butler, A., et al., *Integrating single-cell transcriptomic data across different conditions,*
2035 *technologies, and species.* Nature Biotechnology, 2018. **36**(5): p. 411-420.
2036 85. Germain, P.-L., A. Sonrel, and M.D. Robinson, *pipeComp, a general framework for the*
2037 *evaluation of computational pipelines, reveals performant single cell RNA-seq*
2038 *preprocessing tools.* Genome Biology, 2020. **21**(1): p. 227.
2039 86. McGinnis, C.S., L.M. Murrow, and Z.J. Gartner, *DoubletFinder: Doublet Detection in*
2040 *Single-Cell RNA Sequencing Data Using Artificial Nearest Neighbors.* Cell Systems,
2041 2019. **8**(4): p. 329-337.e4.
2042 87. McCarthy, D.J., et al., *Scater: pre-processing, quality control, normalization and*
2043 *visualization of single-cell RNA-seq data in R.* Bioinformatics, 2017. **33**(8): p. btw777.
2044 88. Zappia, L. and A. Oshlack, *Clustering trees: a visualization for evaluating clusterings at*
2045 *multiple resolutions.* GigaScience, 2018. **7**(7): p. giy083.
2046 89. Phipson, B., et al., *propeller: testing for differences in cell type proportions in single cell*
2047 *data.* Bioinformatics, 2022. **38**(20): p. 4720-4726.
2048 90. Carpenter, A.E., et al., *CellProfiler: image analysis software for identifying and*
2049 *quantifying cell phenotypes.* Genome Biology, 2006. **7**(10): p. R100.

2050